MARTIN MARIETTA ENERGY SYSTEMS LIBRARIES

3 4456 0274852 4

ORNL/TM-10665

ornl

OAK RIDGE NATIONAL LABORATORY

MARTIN MARIETTA

Thermal Analysis of Heat Storage Canisters for a Solar Dynamic, Space Power System

R. P. Wichner
A. D. Solomon
J. B. Drake
P. T. Williams

OAK RIDGE NATIONAL LABORATORY
CENTRAL RESEARCH LIBRARY
CIRCULATION SECTION
4500N ROOM 175
LIBRARY LOAN COPY
DO NOT TRANSFER TO ANOTHER PERSON
If you wish someone else to see this report, send in name with report and the library will arrange a loan.

OPERATED BY
MARTIN MARIETTA ENERGY SYSTEMS, INC.
FOR THE UNITED STATES
DEPARTMENT OF ENERGY

Printed in the United States of America. Available from
National Technical Information Service
U.S. Department of Commerce
5285 Port Royal Road, Springfield, Virginia 22161
NTIS price codes—Printed Copy: A04; Microfiche A01

This report was prepared as an account of work sponsored by an agency of the United States Government. Neither the United States Government nor any agency thereof, nor any of their employees, makes any warranty, express or implied, or assumes any legal liability or responsibility for the accuracy, completeness, or usefulness of any information, apparatus, product, or process disclosed, or represents that its use would not infringe privately owned rights. Reference herein to any specific commercial product, process, or service by trade name, trademark, manufacturer, or otherwise, does not necessarily constitute or imply its endorsement, recommendation, or favoring by the United States Government or any agency thereof. The views and opinions of authors expressed herein do not necessarily state or reflect those of the United States Government or any agency thereof.

ORNL/TM-10665

THERMAL ANALYSIS OF HEAT STORAGE CANISTERS FOR A SOLAR DYNAMIC, SPACE POWER SYSTEM*

R. P. Wichner†
A. D. Solomon‡
J. B. Drake‡
P. T. Williams**

---

*Work performed for NASA LeRC, Space Station Program under Contract C-31002-J.

†Engineering Technology Division, ORNL

‡Engineering Physics and Mathematics Division, ORNL

**Computer and Telecommunications Division, Martin Marietta Energy Systems, Inc.

Date Published - April 1988

Prepared by the
OAK RIDGE NATIONAL LABORATORY
Oak Ridge, Tennessee 37831
operated by
MARTIN MARIETTA ENERGY SYSTEMS, INC.
for the
U.S. DEPARTMENT OF ENERGY
under Contract No. DE-AC05-84OR21400

MARTIN MARIETTA ENERGY SYSTEMS LIBRARIES

3 4456 0274852 4

CONTENTS

	Page
ACKNOWLEDGMENT	v
ABSTRACT	1
1. INTRODUCTION	1
1.1 Objectives and Scope	1
1.2 Geometry and Boundary Conditions	4
1.3 Salt Properties	7
2. THERMAL ANALYSIS METHODS	8
2.1 Solidification Front Analysis	8
2.2 Finite Difference Grid and Equations	11
3. VOID EFFECTS	18
3.1 Behavior in 1-g and 0-g	18
3.2 Heat Transfer Across the Void	20
4. LIQUID VELOCITY DETERMINATION	23
4.1 Incentive for Determination of Liquid Velocities	23
4.2 Method for Determining Liquid Velocities	24
5. RESULTS	27
6. CLOSING	45
7. NOMENCLATURE	47
8. REFERENCES	49

ACKNOWLEDGMENT

The authors gratefully acknowledge the advice and comments provided by Vasilios Alexiades of the Department of Mathematics of the University of Tennessee and by D. G. Wilson of the Engineering Physics and Mathematics Division. The work was performed for the Space Station Systems Directorate, Solar Dynamic Power Module Division, NASA Lewis Research Center. We also would like to acknowledge the helpful support that Steve Johnson, NASA LeRC, provided to us throughout the project.

THERMAL ANALYSIS OF HEAT STORAGE CANISTERS FOR A SOLAR DYNAMIC, SPACE POWER SYSTEM

R. P. Wichner
A. D. Solomon
J. B. Drake
P. T. Williams

ABSTRACT

A thermal analysis was performed of a thermal energy storage canister of a type suggested for use in a solar receiver for an orbiting Brayton cycle power system. Energy sotrage for the eclipse protion of the cycle is provided by the latent heat of a eutectic mixture of LiF and CaF_2 contained in the canister. The chief motivation for the study is the prediction of vapor void effects on temperature profiles and the identification of possible differences between ground test data and projected behavior in microgravity. The first phase of this study is based on a two-dimensional, cylindrical coordinates model using an interim procedure for describing void behavior in 1-g and microgravity. The thermal analysis includes the effects of solidification front behavior, conduction in liquid/solid salt and canister materials, void growth and shrinkage, radiant heat transfer across the void, and convection in the melt due to Marangoni-induced flow and, in 1-g, flow due to density gradients. A number of significant differences between 1-g and 0-g behavior were found. The resulted from differences in void location relative to the maximum heat flux and a significantly smaller effective conductance in 0-g due to the absence of gravity-induced convection.

1. INTRODUCTION

1.1 Objectives and Scope

The principal objective of this work is to perform a detailed thermal analysis of a heat storage canister of the type currently considered for space power Brayton cycle systems. Attempts are made to develop detailed and realistic temperature profiles and histories with specific emphasis on the effects of the vapor void which develops during the freezing phase for all fluoride salt phase change materials

(PCM's). A second major objective is to link the thermal analysis code with a finite element stress analysis program to determine the resulting thermal stresses and ultimately, the predicted life of the canister. This paper reports on the first phase of the thermal analysis portion of the work.

The thermal storage arrangement considered here is one in which annular-shaped canisters containing a fluoride salt phase change material — a eutectic mixture of LiF and CaF_2 — are stacked around tubes in the receiver. A He-Xe gas mixture containing 28 vol-% Xe is passed through these tubes before entry to the turbine (Fig. 1).[1] Both the temperature of the heat sink (i.e., the gas in the tubes) and the solar heating rate on the exterior of the canister vary with cycle time. Moreover, the solar heat flux is not uniform around the periphery of the tube, peaking in the direction facing the center of the receiver and becoming significantly lower along the surface which faces the receiver wall.

Accurate portrayal of the temperature behavior in such a system requires that a number of concurrent phenomena be taken into account. Motion of the solidification front affects the heat balance and the heat

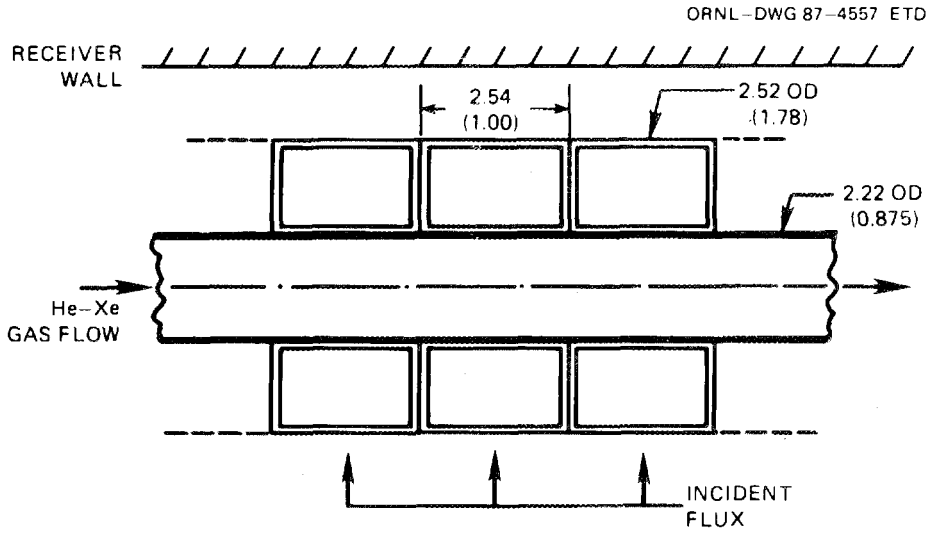

Fig. 1. Arrangement of PCM canisters on He-Xe tubes (dimensions in cm (in).

transport behavior due both to thermal conductance differences between the liquid and solid and the availability of liquid volume for convection. In addition, vapor void formation occurs, common to all fluoride PCM systems, resulting from the higher density of the solid relative to the liquid. Thus a three phase system exists within the canister in which the solid and vapor phases grow during cooling, and the liquid phase grows on heating.

Heat transport through the solid phase is assumed to occur solely by conduction*, however, convection can be a significant transport mechanism in the liquid phase. This is especially true at times approaching sunset when the maximum degree of melting occurs, and in a gravity field, which provides a body force for density-driven currents. At these temperature levels (~1050 K) radiation clearly dominates conduction as the heat transfer mechanism across the void. However, for situations where voids are totally enclosed in liquid, a vaporization/condensation mode of heat transport across the void may be competitive with radiation.

For this first phase of the thermal analysis, a number of simplifying assumptions have been made which will be refined in the course of model development work for NASA's Advanced Solar Dynamic Program. Most importantly, a two dimensional, $r-\theta$ geometry was assumed with essentially constant conditions along the direction of the canister axis. This less than satisfactory assumption for a strongly 3-D situation was found to be essential as a model development stage while still providing early temperature profile estimates for the receiver designers. In addition, the size and location of the void in 1-g and microgravity is determined by an interim procedure described in part 3.1.

In summary, the heat transport mechanisms and phenomena that are taken into account in the analysis are the following: (1) liquid/solid phase front motion, (2) vapor void location, size and shape, by an interim, empirical procedure, (3) heat conduction in the solid phase,

---

*Samples of $LiF-CaF_2$ solid appear to be nearly opaque however, significant radiant transmission through liquid salt is possible.

(4) convective flow in the liquid phase driven by surface tension variation along the void surface, and additionally in 1-g by bouyancy effects, (5) convective and conductive heat transport in the liquid, and (6) radiative heat transport across the void.

1.2 Geometry and Boundary Conditions

Information regarding canister geometry, materials, insolation rates as a function of time and the distribution of the incident heat flux around the canister were provided by NASA Lewis Research Center.[2] The specific configuration depicted in Fig. 1 on which the analysis is based was developed by Rocketdyne under contract from NASA Le-Rc.1 The arrangement of the annular canisters surrounding the gas heating tubes in the receiver is shown in Fig. 1. Each canister is 2.54 cm (1.0 in.) long and has a 4.52-cm (1.78-in.) OD. The OD of the interior tube is 2.22 cm (0.875 in.). Thus, the volume within the canister is 21.2 cm^3, which if completely filled with liquid salt would contain 44.5 gm of PCM. The higher density of the solid (see Table 1) would for these conditions result in a 4.6 cm^3 vapor void in the fully frozen state or approximately 22% of the canister volume. A He-Xe gas mixture enters the receiver tube at 811 K (1000°F) to be heated to a nominal exit temperature of 1033 K (1400°F). In actuality, gas temperatures in the receiver tubes vary somewhat during the heating and cooling cycle. The mass flow rate of ~9.4 g/s in the tube results in a heat transfer coefficient of ~145 ($W/m^2 \cdot K$).

Thermal analyses were performed for three locations along the tube. Results are reported here for a location about three-quarters of the distance from the inlet to the exit where the gas temperatures and heat fluxes are given in Fig. 2. The cycle time is ~92 min with a heat flux at this location of ~1 (W/cm^2) for a large portion of the insolation period. During the shadow phase, gas temperatures fall from a maximum value of ~1050 K at sunset to minimum during shadow of ~975 K. It is also noteworthy that the heat flux during the eclipse portion of the cycle becomes quite negative at this location, reradiating to cooler

Table 1. $LiF-CaF_2$ Salt Properties Near the Melt Temperature (Ref. 2) (1040 K)

Property		
mol% CaF_2		19.5
melt temperature	K	1040
Latent heat	J/g	815
Solid density	g/cm^3	2.68
Liquid density	g/cm^3	2.10
$\frac{v_S - v_L}{v_L}$		-0.216
Specific heat, solid	J/g•K	1.76
Specific heat, liquid	J/g•K	1.76
Thermal conductivity, solid	W/cm•K	0.040
Thermal conducticity, liquid	W/cm•K	0.016
Viscosity	poise	0.022
Surface tension (γ)[a]	$ergs/cm^2$	244
$d\gamma/dT$[a]	$ergs/cm^2 \cdot K$	9.9×10^{-2}

[a] LiF properties (Ref. 21).

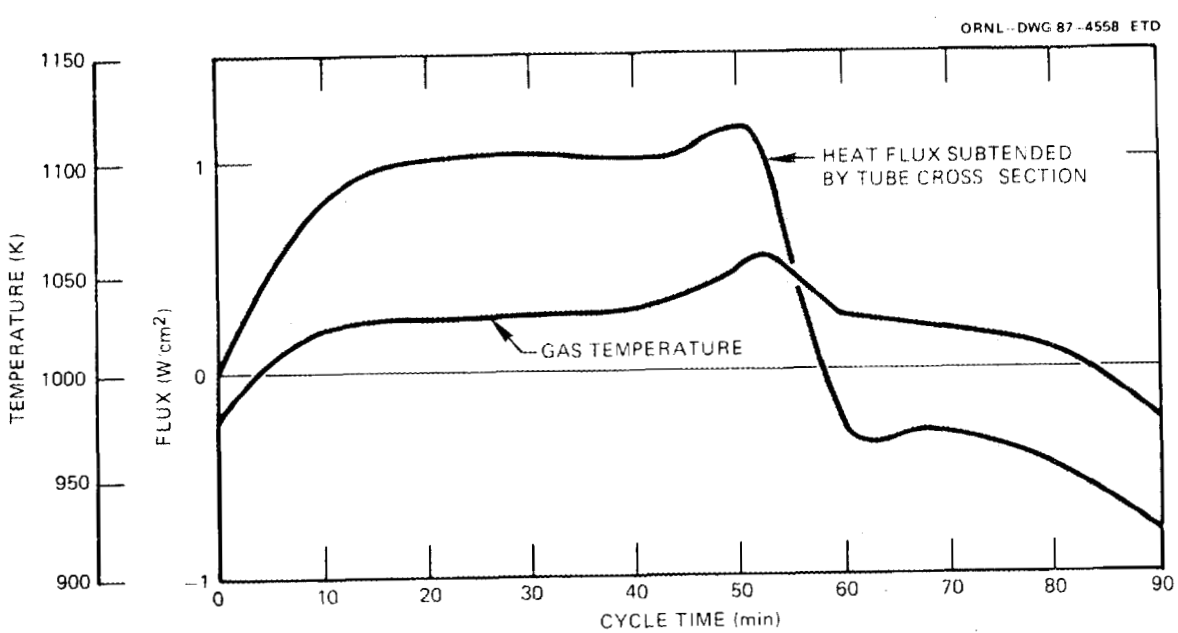

Fig. 2. Canister boundary conditions.

portions of the receiver at a rate of up to 75% of the maximum insolation rate. The maximum insolation rate in the receiver is ~2 (W/cm^2) and occurs nearer the gas inlet.

The heat flux subtended by the canister cross-section is distributed peripherally in the manner shown in Fig. 3. A higher thermal flux exists along the canister surface facing the interior of the receiver relative to the back face. The heat flux along the canister surface facing the receiver wall results from thermal radiation passing between the canisters and reradiating from the back wall. The peripheral flux distribution is approximated along the front face by,

$$q_{front}(\theta,t) = (0.54 \cos \theta + 0.29)\, q(t) \tag{1.1}$$

where the $\theta = 0$ direction is defined as being in the direction of the

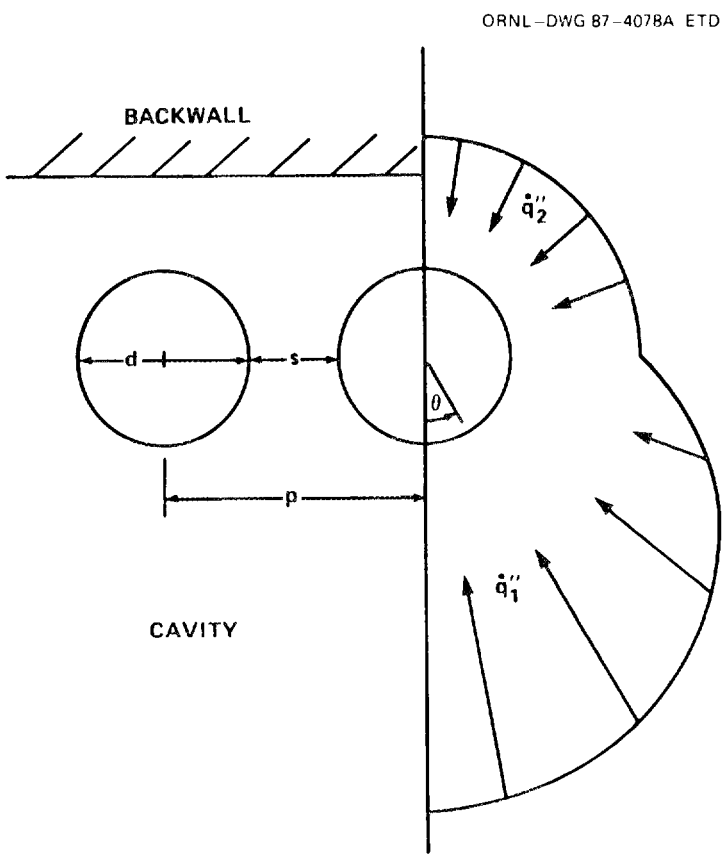

Fig. 3. Heat flux around canister.

receives centerline and q(t) is the heat flux subtended by the canister cross-section. The heat flux on the rear face ($90° < \theta < 270°$) was assumed to be constant with θ and equal at each time, t, to the heat flux directed into the gap between adjacent canisters, (i.e., the gap, s, in Fig. 3). The result in

$$q_{rear}(t) = 0.29\ q(t)\ . \tag{1.2}$$

The boundary conditions for the 2-D analysis are specified by the following: (1) the heat flux along the exterior surface, which varies with time as shown in Fig. 2 and with peripheral location as defined by Eqs. (1.1) and (1.2), (2) the gas temperature in the interior tube, varying with time as shown in Fig. 2, and (3) the insulated sidewall faces.

1.3 Salt Properties

Except where indicated, the properties of the salt used as the latent heat storage medium, given in Table 1, were provided by NASA LeRc.[2] The melting temperature of the $LiF-CaF_2$ eutectic is 1040 K with an estimated latent heat of 815 (J/g). Note that the higher density of the solid would cause a vapor void to form on freezing equal to 21.6% of the canister volume, assuming it to be completely full as a liquid. Values of the surface tension and the rate of variation of the surface tension with temperature, the parameter which drives the Marangoni flow, are not available for this salt mixture. Values for these parameters were therefore taken as those for pure LiF.

2. THERMAL ANALYSIS METHODS

2.1 Solidification Front Analysis

The various approaches towards specification of a transient melt-freeze front may be classified as follows: (1) exact analytical solutions, (2) approximation methods applied to obtain analytical solutions, (3) strong numerical methods, and (4) weak numerical methods. A discussion regarding the general applicability and limitations of each type of approach is provided by Solomon et al.[3] Briefly, analytical approaches, both exact and approximate, are limited to relatively simple systems, usually to only one space dimension and to steady or regularly varying boundary conditions which avoid periodic or multiple phase fronts. Analytical approaches are therefore useful for preliminary or scoping evaluations but rarely find application for any realistic situation except for idealized experimental situations. Most of the numerical solutions fall in the category of so-called "strong numerical solutions", wherein the time varying coordinates of the phase boundary are precisely specified by a heat balance across the boundary. These methods also apply only to relatively simple situations at best, and with some difficulty to two-dimensional systems with non-periodic boundary conditions. Strong numerical solutions become intractable for more complex situations involving three dimensions or periodic boundary conditions which could generate complex or re-entrant phase boundary configurations.

In contrast, so-called "weak numerical solutions" do not pay explicit attention to the location of the phase boundary. Of the various types of weak solutions available, the type designated as the "enthalpy method" appears to be most suitable to ultimately evolve into a generally applicable approach, i.e., one that may be employed with three-dimensional curvilinear coordinates and with periodic or irregular boundary conditions which generate complex phase boundary configurations. The "enthalpy method" has been described in several recent publications;[3,4] briefly, the method may be characterized as follows:

An energy balance on a volume element may be written:

$$\frac{\partial}{\partial t}(\rho^{\alpha} e) = -\nabla\cdot(k^{\alpha}\nabla T) - \nabla\cdot\vec{v}\rho^{\alpha} e \tag{2.1}$$

where,

e = enthalpy per unit mass,
ρ^{α} = density of phase α in the volume element,
k^{α} = thermal conductivity of phase α in the volume element,
$\vec{v}$ = liquid velocity,
T = temperature of fluid in the volume element,
α = assigned liquid, solid, or "mushy".

In the explicit numerical scheme used in this study, Eq. (2.1) is used to update values of e in each volume element based on the map of k^{α}, T, $\vec{v}$, ρ^{α}, and e's from the preceding time step. The value of e may be altered due to conduction or convection as indicated by the terms on the right. (As noted below, $\vec{v}$ is induced by surface tension variation along the liquid-vapor interface and, in a gravity field, by the gravity body force working on a liquid density variation.)

The essence of the "enthalpy" method is to determine the state within each control volume according to updated values of the specific enthalpy, e. Referencing e to the value for the solid at the melt temperature T_m, yields negative values of e for the solid below the melting point,

$$e = c^S (T - T_m) \ . \tag{2.2}$$

For the so-called "mushy" elements which contain both liquid and solid, both assumed to be at T_m, the specific enthalpy is given by,

$$e = x\ \Delta H_m \ , \tag{2.3}$$

where x is the mass fraction molten, and ΔH_m is the heat of fusion per mass. In liquid elements, the specific enthalpy is determined by,

$$e = \Delta H_m + c^L (T - T_m) \ . \tag{2.4}$$

Since the amount of mass in each element varies with the temperature, the total energy balance is performed by determining the energy in each volume element by

$$E = \rho e V \ , \tag{2.5}$$

where ρ is the average density of the mass in the element of volume, V. It is assumed for this illustration that V is constant throughout the grid. In general, V varies, and its variation is accounted for in the finite difference equations. In the present cast, ρ was assigned constant values ρ^S and ρ^L for solid and liquid elements and averaged in the mushy elements,

$$\rho^m = (1 - \varepsilon_L)\ \rho^S + \varepsilon_L \rho^L \ , \tag{2.6}$$

where ε_L is the volume fraction liquid in the central volume.

In addition, the effective thermal conductivity of the elements, k^m, must be evaluated based on k^S, k^L and the liquid fraction, x. Clearly, there is no precise method for determining k^m since it depends on the unknown configuration of liquid and solid phases within the mushy element. The usual procedure is to simply mass-average k_m as for ρ^m which at least places k^m between the known limits k^S and k^L.

An explicit time integration scheme is used to determine updated values of the specific enthalpy, e, based on the existing temperature and phase map, and then to assign new state parameters, c, ρ, x and T according to the new values of e and the rules prescribed by Eqs. (2.2) through (2.6). Negative values of e denote solid-containing control volumes; ρ^S, c^S, and k^S are assigned to these elements. Values of e in excess of ΔH_m denote all-liquid control elements into which properties ρ^L, c^L and k^L are assigned. Values of e between 0 and ΔH_m denote "mushy" control volumes. For these, the value of x is determined from Eq. (2.3), and averaged property parameters, ρ^m, c^m and k^m are assigned. In addition, the control element temperature is determined from the value e, using Eqs. (2.2) and (2.4) for identified solid and

liquid elements, respectively. The temperature of mushy elements are assumed to be equal to T_m.

The disadvantage of this procedure is that the phase boundaries are not clearly determined in a coarse grid and, to a lesser degree, an uncertainty in the temperature profile is caused by use of an approximate value of the effective thermal conductivity in the mushy zone. However, these disadvantages are minor compared with the great advantage of permitting the numerical procedure to proceed continuously through the grid without explicit solution for the phase boundary. In any case, the phase boundary may be located with any desired precision by reduction of mesh size, a process in which it may be shown the numerical solution converges to the analytical solution.

2.2 Finite Difference Grid and Equations

The mesh employed for the thermal calculations is shown in Fig. 4 superimposed on the finite element grid used in the calculation of canister stresses. Figure 5 illustrates typical neighboring nodes used for defining terms in the finite difference equations. In Fig. 4, the PCM regime is subdivided into eight radial and 16 circumferential control volumes and one additional radial node for the inner and outer sections of the canister wall. The finite element grid (used for the associated stress calculation) is offset by one-half of an element width in both the r- and θ-directions so that the four corners of each interior finite element coincide with a thermal node. The canister surfaces, however, are set to coincide with the radial boundaries of both the thermal and finite element meshes, the radial offset in the two being established by including half-width finite elements adjacent to the canister wall elements. This sort of a half-width offset of the two grids enables direct transfer of temperatures, computed for the center of each thermal control volume, to the finite element grid which requires temperatures at each corner.

The finite difference approximations used for interior and boundary control elements are listed in Table 2 in terms of $E_{i,j}$, the total

Table 2. Finite Difference Equations (Refer to Fig. 5)

Interior Node

$$\frac{E^{n+1}_{i,j} - E^{n}_{i,j}}{\Delta t} = r_{i,j} + \frac{\Delta r}{2} \; \Delta\theta \; \Delta z \; \frac{T^{n}_{i+1,j} - T^{n}_{i,j}}{\frac{\Delta r}{2} \; \frac{1}{k_{i,j}} + \frac{1}{k_{i+1,j}}}$$

$$- \frac{1}{2} \left[(h^{n}_{i+1,j} + h^{n}_{i,j}) \; u^{n}_{i+1,j} - \alpha (h^{n}_{i+1} - h^{n}_{i,j}) \left| u^{n}_{i+1,j} \right| \right]$$

$$+ (r_{i,j} - \frac{\Delta r}{2}) \; \Delta\theta \; \Delta z \; \frac{T^{n}_{i-1,j} - T^{n}_{i,j}}{\frac{\Delta r}{2} \; \frac{1}{k_{i,j}} + \frac{1}{k_{i-1,j}}}$$

$$+ \frac{1}{2} \left[(h^{n}_{i-1,j} + h^{n}_{i,j}) \; u^{n}_{ij} - \alpha (h^{n}_{i,j} - h^{n}_{i-1,j}) \left| u^{n}_{i,j} \right| \right]$$

$$+ \Delta r \; \Delta z \; \frac{T^{n}_{i,j-1} - T^{n}_{i,j}}{r_{i,j} \; \frac{\Delta\theta}{2} \; \frac{1}{k_{i,j}} + \frac{1}{k_{i,j-1}}}$$

$$+ \frac{1}{2} \left[(h^{n}_{i,j} + h^{n}_{i,j-1}) \; v^{n}_{i,j} - \alpha (h^{n}_{i,j} - h^{n}_{i,j-1}) \left| v^{n}_{i,j} \right| \right]$$

$$+ \Delta r \; \Delta z \; \frac{T^{n}_{i,j+1} - T^{n}_{i,j}}{r_{i,j} \; \frac{\Delta\theta}{2} \; \frac{1}{k_{i,j}} + \frac{1}{k_{i,j+1}}}$$

$$- \frac{1}{2} \left[(h^{n}_{i,j+1} + h^{n}_{i,j}) v^{n}_{i,j+1} - \alpha (h^{n}_{i,j+1} - h^{n}_{i,j}) \left| v^{n}_{i,j+1} \right| \right]$$

Table 2. (cont.)

Boundary Node - Inner Canister and Pipe

$$\frac{E^{n+1}_{4,j} - E^{n}_{4,j}}{\Delta t} = (r_{4,j} + \frac{\Delta r}{2})\ \Delta\theta\ \Delta z\ \frac{T^{n}_{5,j} - T^{n}_{4,j}}{\frac{\Delta r}{2}\ \frac{1}{k_{4,j}} + \frac{1}{k_{5,j}}}$$

$$- \frac{1}{2}\ [(h^{n}_{5,j} + h^{n}_{4,j})\ u^{n}_{5,j} - \alpha(h^{n}_{5,j} - h^{n}_{4,j})|u^{n}_{5,j}|]$$

$$+ (r_{4,j} - \frac{\Delta r}{2})\ \Delta\theta\ \Delta z\ \frac{(T^{n}_{fluid} - T^{n}_{4,j})}{\frac{\Delta r/2}{k_{4,j}} + \frac{1}{h_{fluid}} + \frac{\Delta r_{can}}{k_{can}} + \frac{\Delta r_{pipe}}{k_{pipe}}}$$

$$+ \Delta r\ \Delta z\ \frac{T^{n}_{4,j-1} - T^{n}_{4,j}}{r_{4,j}\ \frac{\Delta\theta}{2}\ \frac{1}{k_{4,j}} + \frac{1}{k_{4,j+1}}}$$

$$+ \frac{1}{2}\ [(h^{n}_{4,j} + h^{n}_{4,j-1})\ v^{n}_{4,j} - \alpha(h^{n}_{4,j} - h^{n}_{4,j-1})|v^{n}_{4,j}|]$$

$$+ \Delta r\ \Delta z\ \frac{T^{n}_{4,j+1} - T^{n}_{4,j}}{r_{4,j}\ \frac{\Delta\theta}{2}\ \frac{1}{k_{4,j}} + \frac{1}{k_{4,j+1}}}$$

$$- \frac{1}{2}\ [(h^{n}_{4,j+1} + h^{n}_{4,j})v^{n}_{4,j+1} - \alpha(h^{n}_{4,j+1} - h^{n}_{4,j})|v^{n}_{i,4+1}|]$$

Table 2. (cont.)

Boundary Node - Outer Canister and Applied Flux

$$\frac{E^{n+1}_{nr,j} - E^{n}_{nr,j}}{\Delta t} = (r_{nr,j} + \frac{\Delta r}{2})\ \Delta\theta\ \Delta z\ \frac{T^{n}_{nr+1,j} - T^{n}_{nr,j}}{\frac{\Delta r}{2}\ \frac{1}{k_{nr,j}}}$$

$$+ (r_{nr,j} - \frac{\Delta r}{2})\ \Delta\theta\ \Delta z\ \frac{T^{n}_{nr-1,j} - T^{n}_{nr,j}}{\frac{\Delta r}{2}\ \frac{1}{k_{nr,j}} + \frac{1}{k_{nr-1,j}}}$$

$$+ \frac{1}{2}\ [(h^{n}_{nr-1} + h^{n}_{nr,j})\ u_{nr,j} - \alpha(h^{n}_{nr,j} - h^{n}_{nr-1,j})|u^{n}_{nr,j}|]$$

$$+ \Delta r\ \Delta z\ \frac{T^{n}_{nr,j-1} - T^{n}_{nr,j}}{r_{nr,j}\ \frac{\Delta\theta}{2}\ \frac{1}{k_{nr,j}} + \frac{1}{k_{nr,j-1}}}$$

$$+ \frac{1}{2}\ [(h^{n}_{nr,j} + h^{n}_{nr,j-1})\ v_{nr,j} - \alpha(h^{n}_{nr,j} - h^{n}_{nr,j-1})|v^{n}_{nr,j}|]$$

$$+ \Delta r\ \Delta z\ \frac{T^{n}_{nr,j+1} - T^{n}_{nr,j}}{r_{nr,j}\ \frac{\Delta\theta}{2}\ \frac{1}{k_{nr,j}} + \frac{1}{k_{nr,j+1}}}$$

$$- \frac{1}{2}\ [(h^{n}_{nr,j+1} + h^{n}_{nr,j})v_{nr,j+1} - \alpha(h^{n}_{nr,j+1} - h^{n}_{nr,j})|v^{n}_{nr,j+1}|]$$

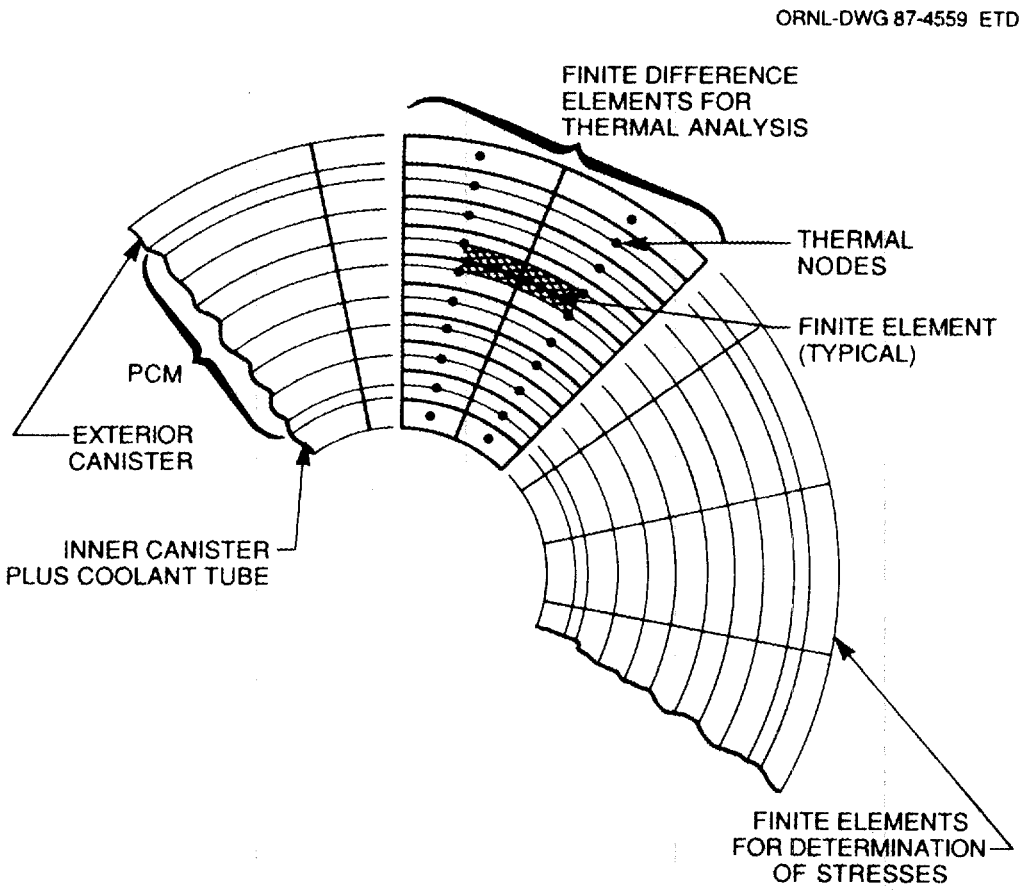

Fig. 4. Finite difference elements and relationship to the finite element grid used for determination of stresses.

enthalpy in control element (i,j), which is related to the specific enthalpy by

$$E_{i,j} = \rho_{i,j} V_{i,j} e_{i,j} \ . \tag{2.7}$$

As noted in Sect. 2.1, values of $e_{i,j}$ are used to determine the state of each control element; at each time step values of $\rho_{i,j}$, $T_{i,j}$ $k_{i,j}$ and $x_{i,j}$ are determined from $e_{i,j}$. Updated values, $E^{n+1}_{i,j}$ are determined from values at the previous time step, $E^{n}_{i,j}$, and the rate of conduction and convection into the control element from adjacent control elements. Table 2 lists the finite difference approximations used for the interior control elements (i.e., those surrounded by PCM elements), and interior

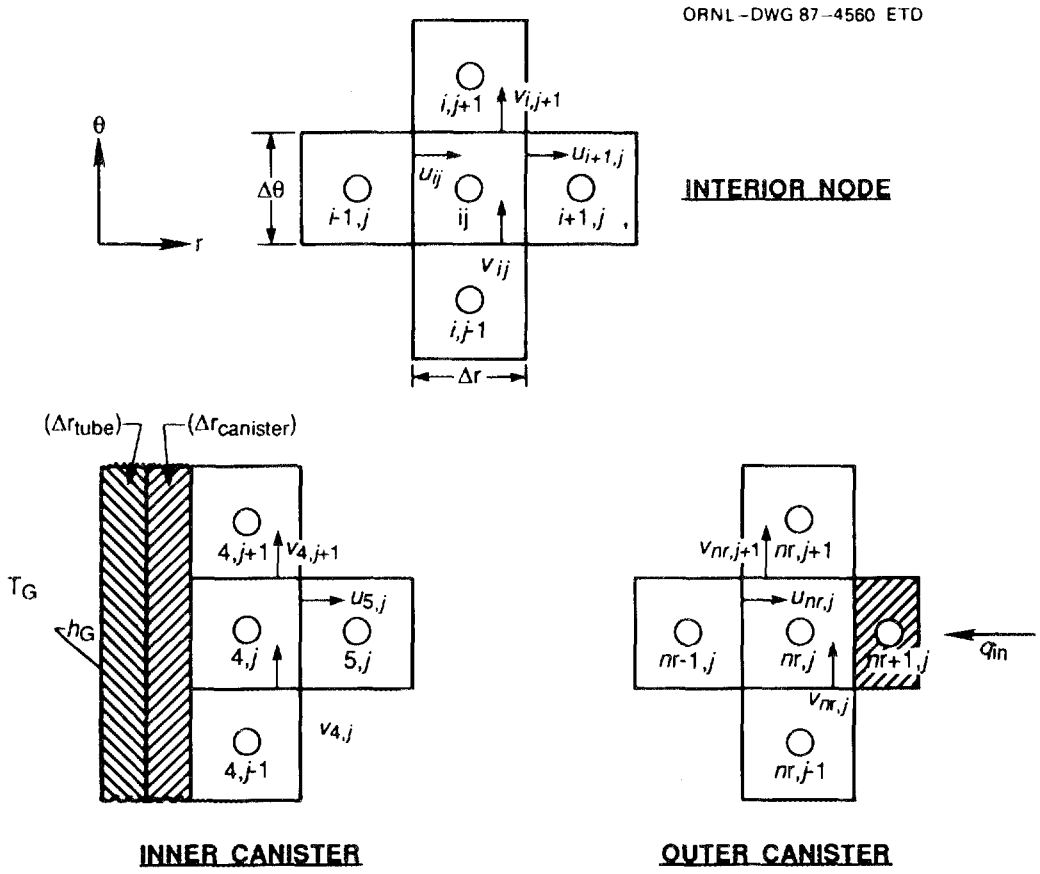

Fig. 5. Illustration of neighboring finite difference control volumes.

and exterior boundary elements for which a canister surface forms a portion of the boundary.

Convective transport rates into the control element are determined by the radial and circumferential velocities u and v, respectively. The velocities in turn are determined by solution of the Navier-Stokes equations for the melt zone as discussed below in Sect. 4. For brevity the term $h_{i,j}$ is used in the convection terms in Table 2 defined as the average enthalpy per unit volume in element (i,j), i.e.,

$$h^n_{i,j} = \rho^n_{i,j} e^n_{i,j} \ .$$

Note from Fig. 5 that the velocities are defined for locations offset from the node by one-half the width of the volume element. Thus the

velocity, $u_{i,j}$ for example, convects material from cell (i-1,j) into (i,j). Ideally the average enthalpy per unit volume,

$$\frac{1}{2}(h_{i-1,j} + h_{i,j}) ,$$

is convected in the r-direction by the velocity $u_{i,j}$.

The convection terms are multiplied by α, a so-called "upwind parameter," which is included to provide numerical stability without resorting to prohibitively small time steps. Since even small flows can cause convection transport to exceed conduction, stability criteria based on conduction rates generally lead to unsuitably large time steps. The upwind parameter is defined by

$$\alpha = \Delta t \max \frac{|u_{max}|}{\Delta r} , \frac{|v_{max}|}{\Delta r \cdot \Delta\theta} , \tag{2.8}$$

$$\alpha \leq 1 .$$

Note, the effect of the addition of the terms multiplied by α is to increase the influence of the upwind control element in the determination of the average value of h being convected.

3. VOID EFFECTS

3.1 Projected Behavior in 1-g and 0-g

A universal feature of energy storage in the latent heat of molten salts is the development of vapor voids during the freezing portion of the thermal cycle due to the generally higher density of the solid. In the present case, the $LiF-CaF_2$ eutectic composition is estimated to have solid and liquid densities of 2.68 and 2.10 g/cm^3, respectively, so that a completely full canister in an all liquid condition would produce a 21.6% void when completely frozen. The projected shape and location of this void is a critical factor in the assessment of temperature profiles in both the salt and canister.

Since there have been no in-situ observations of void behavior under realistic heat storage conditions, the projected behavior is somewhat uncertain. However, post-test observations of melts in 1-g generally show single, lenticular voids that are not inconsistent with emplacement in the highest vertical locations permitted by the freeze-front configuration.[5-7] There have been no equivalent observations for freezing in a microgravity environment. For this situation, it seems reasonable to assume that the void moves so as to minimize interfacial energy. If the liquid-solid components of the interfacial energy are small compared with that of the liquid-vapor surface, this principle would emplace the void in the highest temperature zone (where the liquid-vapor surface energy is the lowest) and in the most compact shape permitted by the solid boundaries formed by the freeze front and container.

This view of void behavior appears to be most likely and was adopted for the calculations; however, it is not without some degree of uncertainty. For example, tests purporting to model the solidification of metals sometime show numerous nucleating sites for voids on the frozen surface being captured by the progressing freeze front.[8] This sort of behavior would lead to a distributed void in the solid and significantly different (and much better) thermal conditions in a heat

storage system. However, this behavior has evidently never been reported to occur with molten salts under approximately realistic heat storage conditions.

In microgravity, there is the additional uncertainty involved in relying on the much smaller surface forces to project void behavior. Though movement of voids towards high temperature zones (hence minimum liquid-vapor surface tension zones) has been clearly established by observation[9,10] and physical principle, the magnitude of the motive force could in some circumstances be significantly less than estimated from pure material values. For example, Thompson, et al.[10] observed the anticipated Marangoni velocities for air bubbles in various organic liquids, but not for air bubbles in water, unless the water was carefully purified. Thus, it appears that surface tension forces in microgravity could be affected by small concentrations of impurities in the melt. An additional uncertainty relates to the attractive force between the liquid and metal container as evidenced by the strongly wetting behavior between molten salt and oxide-free metal surfaces. If this were significant compared with liquid-vapor effects, energy minimization would tend to establish a maximum liquid-solid surface area (as opposed to a minimum liquid-vapor surface) which is perhaps the cause of the annular-shaped voids observed in NASA fuel tank tests under some conditions.[11]

Ultimately, the thermal model should include a rational void behavioral model based on estimates of the relevant forces which effect its position and shape. However, in this interim phase of the work, an ad-hoc procedure was imposed on the calculation prescribing void location and shape according to the rules outlined above. Following each time step, the liquid, solid and "mushy" fields are scanned to determine the total condensed volume and hence, by difference, the total void volume. In 1-g, the estimated void volume was apportioned in top down fashion; i.e., by selecting those elements available for void with maximum values of $r_i \cos \theta_j$, where r_i and θ_j are the nodal coordinates, referring the θ-direction to the vertical and r increasing toward the

outside diameter. This procedure develops an as-flat-as-possible void positioned at an uppermost elevation.

For the 0-g cases, the void was assumed to be located at the position of maximum heat flux and to assume a minimum surface to volume ratio shape, in accord with the notion that Marangoni forces would impel it to the highest temperature location and the surface tension would tend to make it spherical. Toward this end, a void positioning strategy was adopted wherein the required void volume at each time step was allocated beginning the highest temperature volume element, i.e., outermost element at the peak flux location and progressing inward. Admittedly, these empirical rules for void behavior are less than satisfactory and were adopted as an interim step to provide a near-term approximation.

3.2 Heat Transfer Across the Void

Scoping calculations were performed to assess the relative contributions of conduction, radiation, and evaporation/condensation mechanisms to the heat transfer across the void. An ideal, slab-shaped void was assumed with the hot boundary maintained at 1200 K and cold surfaces assumed to range from 1100 to 1200 K. As seen in Fig. 6, radiant heat exchange would range up to ~3.4 (W/cm^2) across this idealized void for the maximum ΔT condition.

Heat transfer across a void could also occur by evaporation and condensation proceeding from the higher to the lower temperature portions of the void surface. Precise description of such a variable temperature void surface could be quite complex. However, an estimated magnitude of the effect may be obtained by (1) assuming a planar void geometry with both liquid surface temperatures set at a temperature, T_2, corresponding void vapor pressure of P_2, and (2) subsequently, one surface is assumed to suddenly achieve a higher temperature, T_1, corresponding higher vapor pressure, P_1. The resulting evaporation rate may

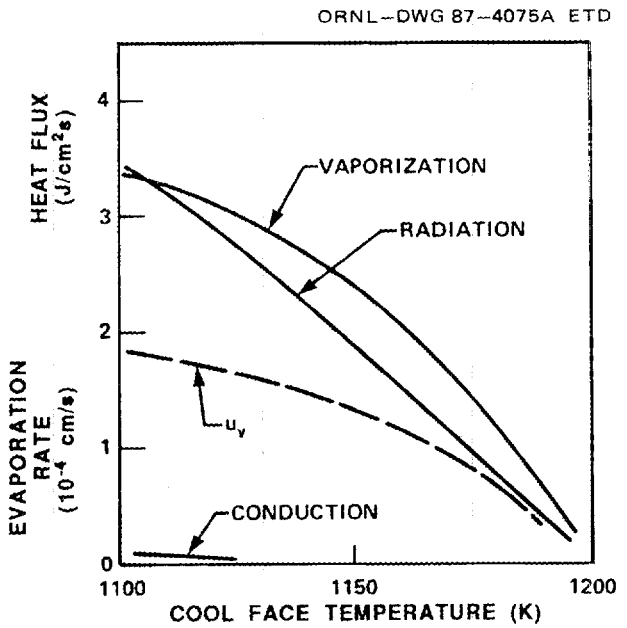

Fig. 6. Comparison of radiant, vaporization and conduction heat fluxes across a planar void with a high temperature face of 1200 K.

reach

$$J_n = \frac{44.3}{\sqrt{T_1 \cdot M_w}} (P_1 - P_2) \ , \tag{3.1}$$

where the numerical constant is appropriate for the flux in $mol/cm^2 \cdot s$, the pressure in atmospheres and temperature in Kelvin.[12] Using vapor pressure and heat of vaporization data for LiF[13] yields the estimated heat fluxes and surface velocities shown in Fig. 6. As seen, heat transport across a void under these conditions via evaporation/condensation may be comparable to radiant transport, provided the void boundary is completely liquid and the assumed idealization corresponds to real behavior. Note, projected surface movements due to evaporation/condensation are quite low, on the order of 10^{-4} cm/s, compared with convective velocities expected from density or surface tension gradients.

Thermal conduction across the void may be shown to be insignificant relative to radiation and vaporization/condensation mechanisms. An

estimate of the value of k_{th} for LiF(g) may be obtained by noting that the kinetic theory of gases predicts it to be independent of pressure and proportional to the quantity $\frac{1}{d}\sqrt{\frac{T}{m}}$, where T, m, and d are respectively the temperature, molecular mass and molecular diameter.[14] Taking as a reference the value for N_2, which has approximately equal molecular mass and, assuming equal collision diameter, yields an estimated k_{th} for LiF(g) at 1000 K of 4.6×10^{-4} W/cm K. Thus a void temperature gradient on the order of 100 K/cm would yield a conductive heat flux of only 0.046 W/cm^2, substantially less than by the other mechanisms. The actual conductive heat flux would be lower still due to the presence of the heavier CaF_2 molecule in addition to LiF.

4. LIQUID VELOCITY DETERMINATION

4.1 Incentive for Determination of Liquid Velocities

Experiments performed by Liu and Meuller[15] on natural convection in horizontal annuli containing various fluids indicate that natural convection becomes a significant factor for heat transfer relative to conduction at a Rayleigh No. of 10^3, and dominates over conduction for Ra > $\sim 10^5$. They found that the ratio of the effective conductivity, k_e, to the molecular conductivity to be given by

$$\frac{k_e}{k} = 0.135 \left(\frac{Pr \cdot Ra}{1.36 + Pr} \right)^{0.278} \tag{4.1}$$

for annuli with gap width to diameter ratios ranging from 0.08 to 3.3 containing air, water and silicone oil and a Ra number range of 300 to 1.8×10^7. A maximum value for the argument in Eq. (4.1) of 10^5 is estimated, corresponding to an effective conductance ratio of 3.3. Thus in 1-g, we would expect heat transfer in the PCM to be accomplished predominantly by natural convection when approaching conditions nearing full melt.

Convection effects in 0-g are expected to be much smaller, though not completely absent. Liquid velocities in 0-g would be driven by surface tension variation along the liquid/vapor interface resulting from temperature gradients. There is no clear indication of the magnitude of such Marangoni-induced convection under these conditions, but calculations by Mankata and Tanasawa[16] for rectangular cavities with one free surface indicate its effect to be significant. For example, they predict an effective conductance ratio, k_e/k, of ~2 for a square cavity with an imposed Marangoni No. of 5×10^3, which is a fairly typical value for the heat storage canister under consideration, assuming the contrary conditions of near complete melting and maximal void size. Since void growth in the canister accompanies the freezing process,

Marangoni-induced convection in 0-g would be expected to be significantly less than this estimate and attain a maximum at some intermediate stage of the melting process.

4.2 Method for Determining Liquid Velocities

Following Chorin's method[17] of time discretization of the incompressible flow Navier-Stokes equation, the time advanced velocities are obtained using a fractional step method. In this method the velocities are advanced using an explicit formula while the pressure is taken implicitly. Taking the pressure implicitly allows exact satisfaction of the continuity equation by the velocity field.

$$\rho \frac{v^{n+1} - v^n}{\Delta t} + \text{grad } p^{n+1} = -v^n \cdot \text{grad } v^n + \text{div } \tau^n + \rho f^n \tag{4.2}$$

This may be viewed as a predictor equation for the velocity v^{n+1}. This equation was used to explicitly advance the velocities, neglecting the pressure term. The predicted velocity will be called v^*, and is given by

$$v^* = v^n + \left(\frac{\Delta t}{\rho}\right) [-v^n \cdot \text{grad } v^n + \text{div } \tau^n + \rho f^n] \tag{4.3}$$

The remaining portion of the time step solves the equation

$$\rho \frac{v^{n+1} - v^*}{\Delta t} + \text{grad } p^{n+1} = 0 \tag{4.4}$$

subject to the continuity requirement of

$$\text{div}(v^{n+1}) = 0 \ . \tag{4.5}$$

Taking the divergence of equation (4.4) and using (4.5) gives an equation for the pressure and a velocity correction equation. The pressure equation is

$$\text{div grad } p^{n+1} = \frac{1}{\Delta t} \text{div } (\rho v^*) \ . \tag{4.6}$$

The velocity correction equation from (4.4) is simply

$$v^{n+1} = v^{*} - \frac{\Delta t}{\rho} \text{grad } p^{n+1}. \tag{4.7}$$

Details of the spacial discretization scheme are described by Drake,[18] and generally follow the staggered mesh, control volume of the SMAC method[19] adapted to cylindrical coordinates.

Boundary conditions for liquid flow along the permanent solid surface follow the standard no-slip condition for velocity and are applied in the usual fashion. The transient, solidification front boundary, however, presents a different situation. Here, the exact location and configuration of the solid surface is not known, in fact is deliberately avoided. An appropriate Navier-Stokes boundary condition procedure is required along the moving surface consistent with the "enthalpy" method principle of avoiding explicit determination of the solidification front. Such a method has been proposed by Drake,[18] the details of which are presented in a forthcoming paper. The essence of Drake's method is to treat each "mushy" volume element as if it were a porous bed of known liquid fraction. In this boundary element forming the transition between liquid and solid, the rules for pressure and velocity variation are artificially set according to packed bed relations wherein the bed porosity is a given function of the liquid fraction, a value that is available from the enthalpy method. The trick is to find a flow equation which reduces to the proper Navier-Stokes form in a fully liquid control element, yields zero velocity in a solid volume element, and provides a transition zone in the mushy element which, though artificial, nevertheless maintains mass and momentum balance. According to Drake, this may be accomplished by the addition of an artificial body force to the momentum equation, such that Eq. (4.2) becomes

$$\rho \frac{v^{n+1} - v^{n}}{\Delta t} + v^{n} \cdot \text{grad } v^{n} - \text{div } \tau^{n} = -\text{grad } p^{n+1} + \rho f^{n} \frac{\mu}{k} v^{n+1} , \tag{4.7}$$

where k is a packed bed permeability according to Darcy's law. This

equation can be applied in both the solid and the liquid provided k is chosen appropriately. In the liquid, the permeability is infinite and hence the term does not contribute to the momentum equation. In the solid the permeability is extremely small, or zero, and this term dominates all others. The effect of this domination will be to drive the velocity in a solid region to zero. When k is in the range of a porous media flow, the convection and diffusion terms will be small and we obtain the Darcy's law equation. Thus by varying the permeability over the fluid domain we can obtain an equation applicable to the entire region. This mathematical device is still in an experimental stage. If proven satisfactory, however, it would provide an advantage for velocity determination of the same nature as the "enthalpy" method provides for temperatures. That is, the numerical procedure may sweep the entire grid without explicitly defining the freeze front boundary.

5. RESULTS

Results are shown for the 1-g cases in Figs. 7 through 14. The temperature and phase maps were plotted using the PATRAN finite element program, which was used in conjunction with the associated finite element stress calculation. The temperature and phase maps (Figs. 7-12) are oriented such that the gravity body force is downward; the maximum solar heat flux is assumed to project upward from below. This arrangement was selected to coincide with an experimental setup at NASA Lewis Research Center. The temperature and phase maps illustrate conditions (1) at sunrise (t = 0), the lowest thermal energy condition, (2) at t = 30 min which is an intermediate temperature during the heating phase, and (3) at t = 50 min, which is about 5 min before sunset, nearing the maximum energy content condition.

Figures 7 and 8 illustrate the temperature and phase location situation at sunrise. As seen from Fig. 2, the time of sunrise follows a period of ~30 min in which the canister experiences a net outward radiant flux at the outer boundary; i.e., the canister is cooled at both the inner and outer surfaces during this period. Hence, the maximum temperature tends to occur in the interior portion, as indicated in Fig. 7, corresponding to the interior "mushy" zone seen in Fig. 8.

Figure pairs 9/10 and 11/12 refer to cycle times of 30 and 50 min, respectively, which are in the heating portion of the cycle. The trend here is toward higher temperatures, increased melting and diminished void volume. Figures 9 and 11 illustrate the unexpected feature that the maximum temperatures are found at the top of the canister despite the fact that the maximum heat flux occurs at the bottom. The cause of this behavior is the flow driven by the 1-g body force convecting hot fluid from the high heat flux zone. The flow pattern observed by viewing velocity maps from consecutive time increments is cyclic in nature, with about a 30 sec period, involving alternately a clockwise and counterclockwise flow pattern. At a time near sundown, Figs. 11 and 12, virtually all temperatures exceed the melting point of 1040 K except for

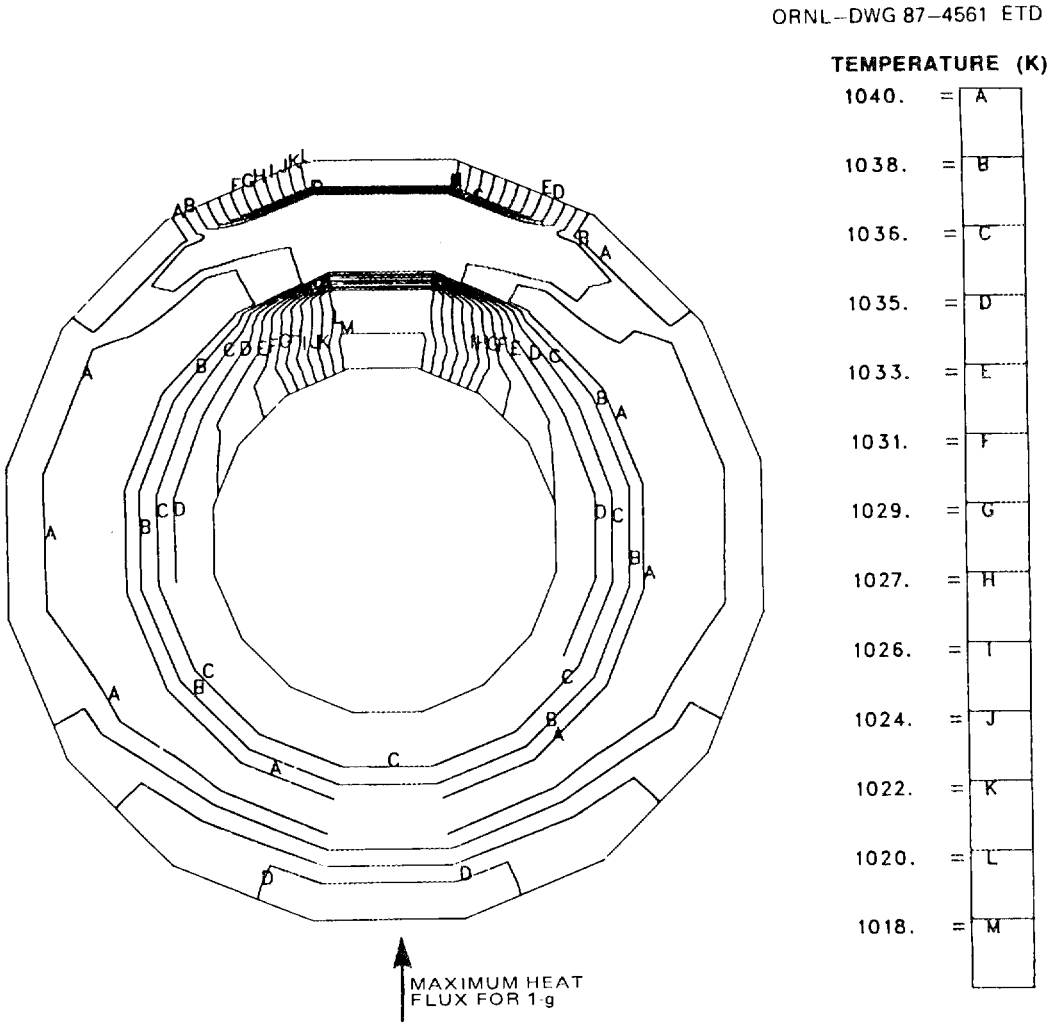

Fig. 7. Temperature contours — 1-g, sunrise (t = 0).

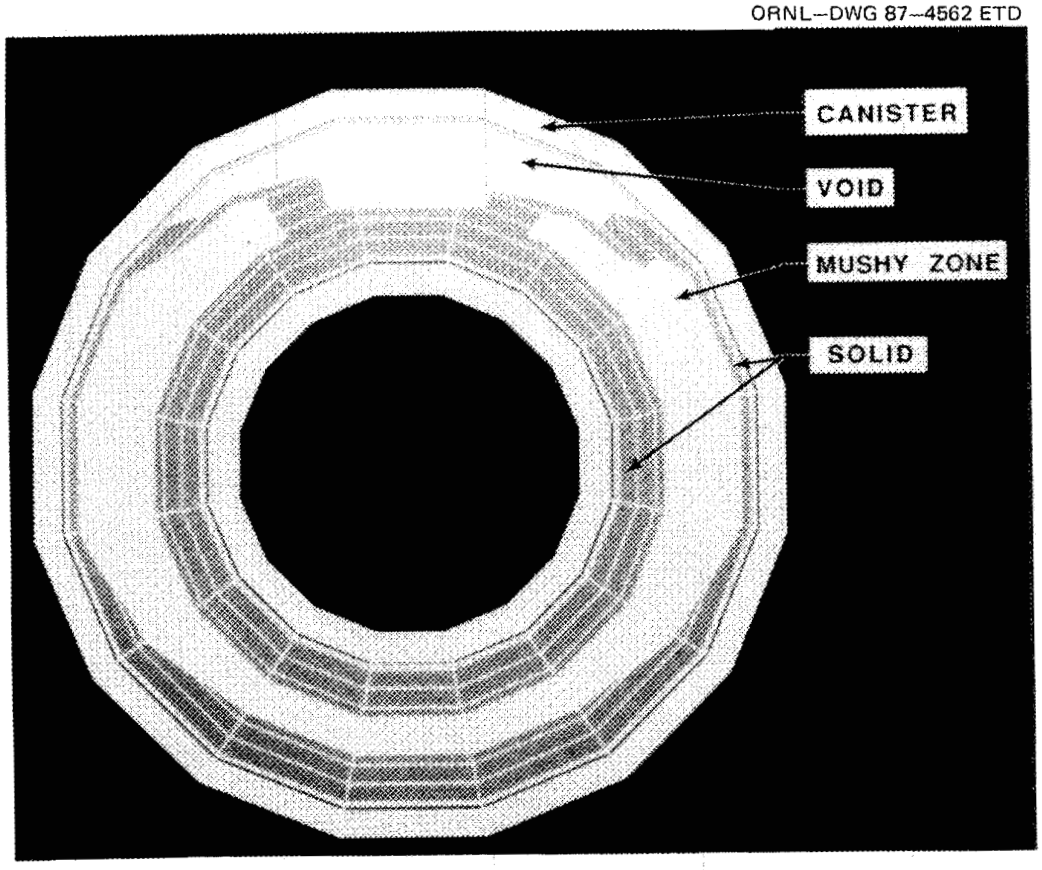

Fig. 8. Phase map — 1-g, sunrise (t = 0).

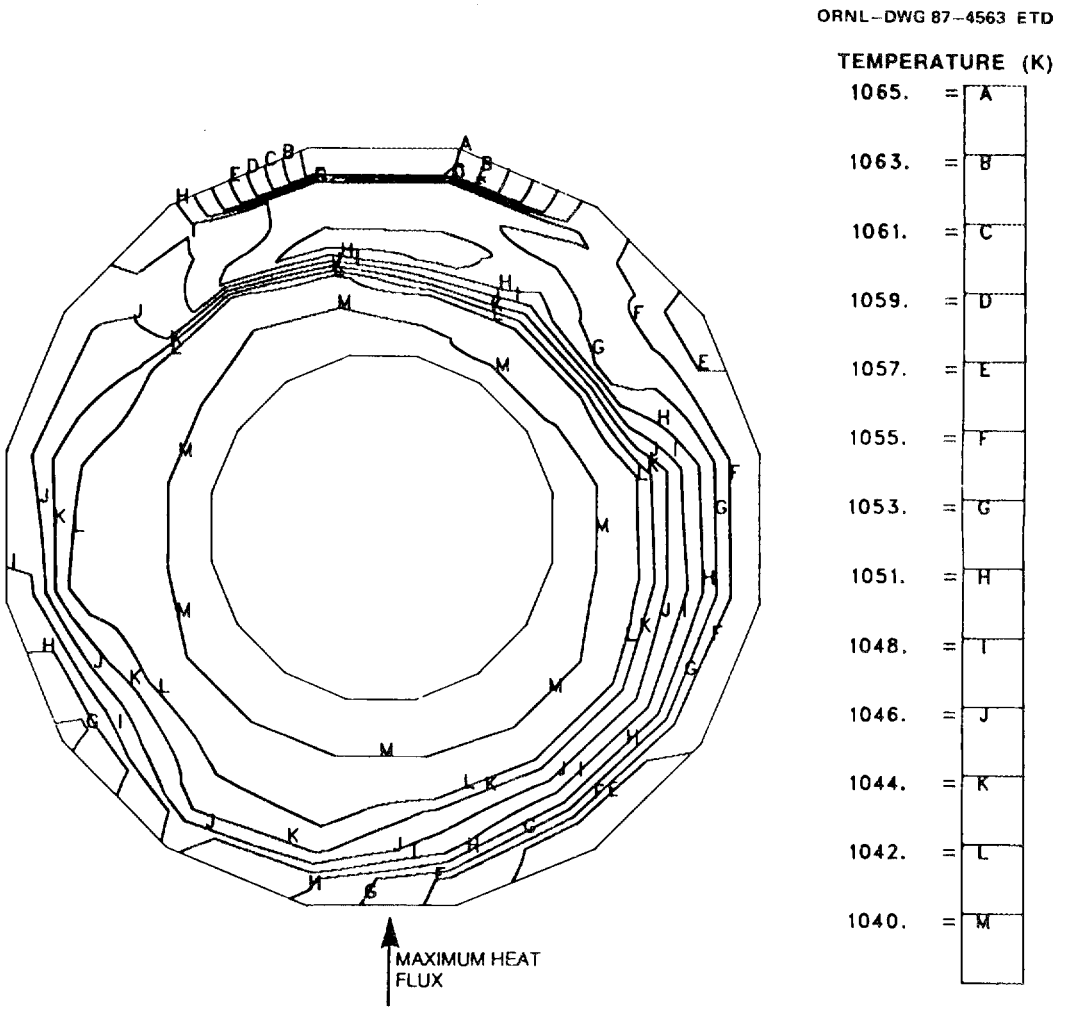

Fig. 9. Temperature contours — 1-g, t = 30 min.

ORNL--DWG 87--4564 ETD

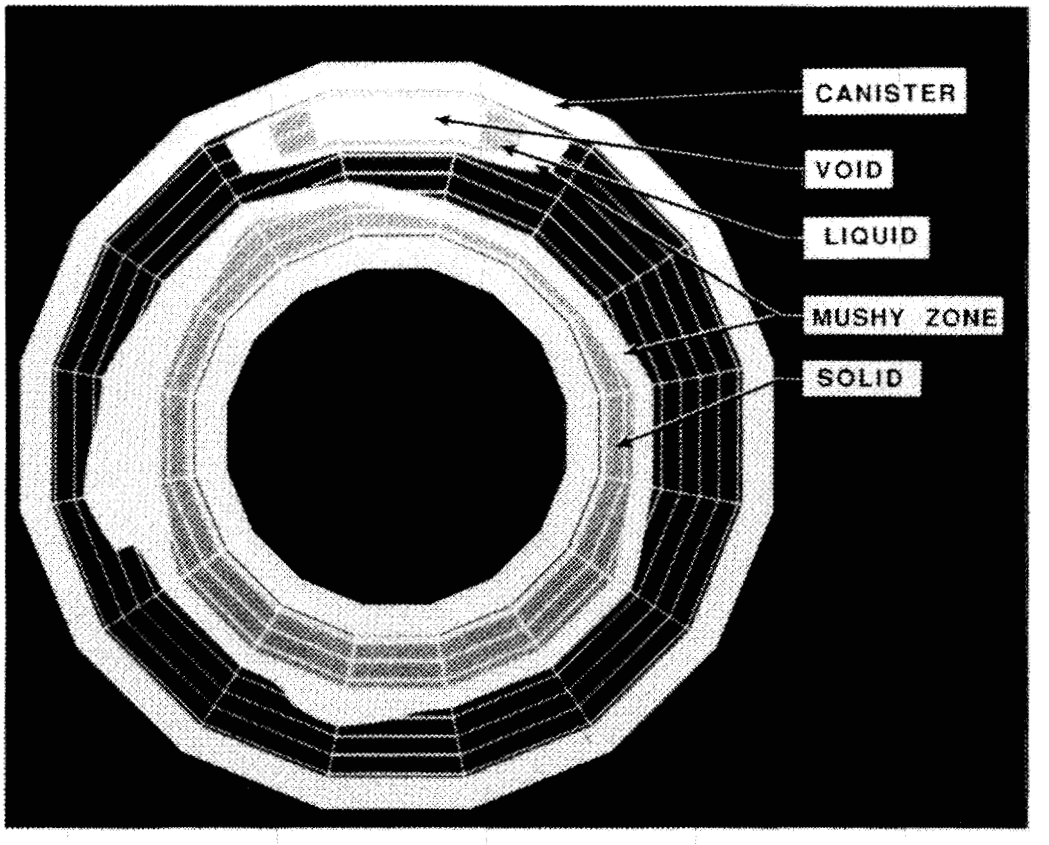

Fig. 10. Phase map — 1-g, t = 30 min.

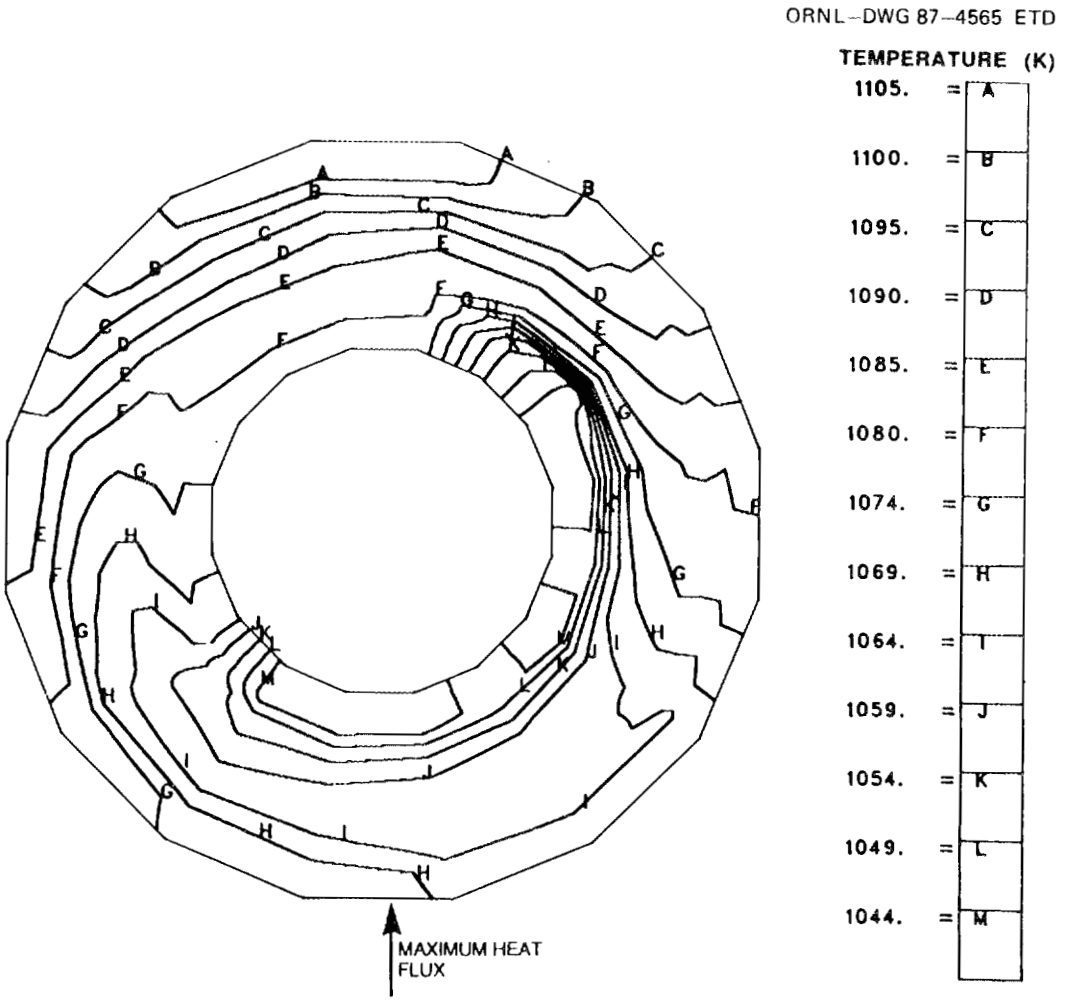

Fig. 11. Temperature contours — 1-g, t = 50 min.

ORNL--DWG 87--4566 ETD

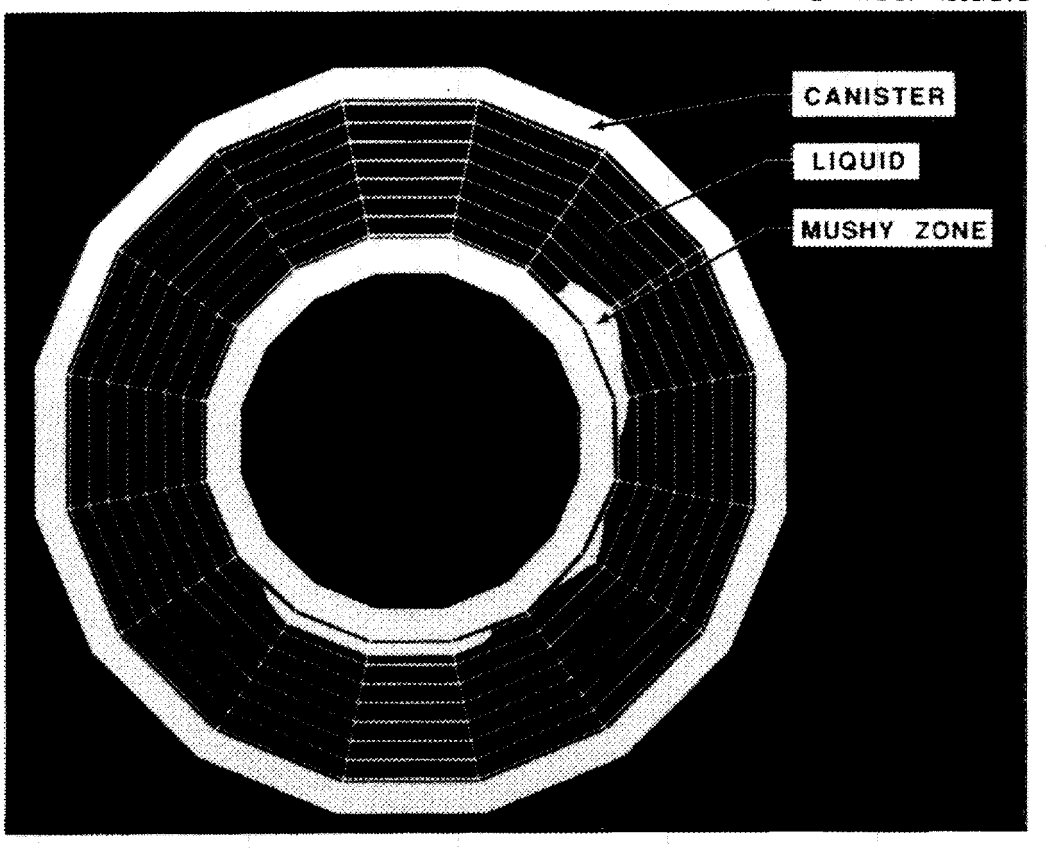

Fig. 12. Phase map — 1-5, t = 50 min.

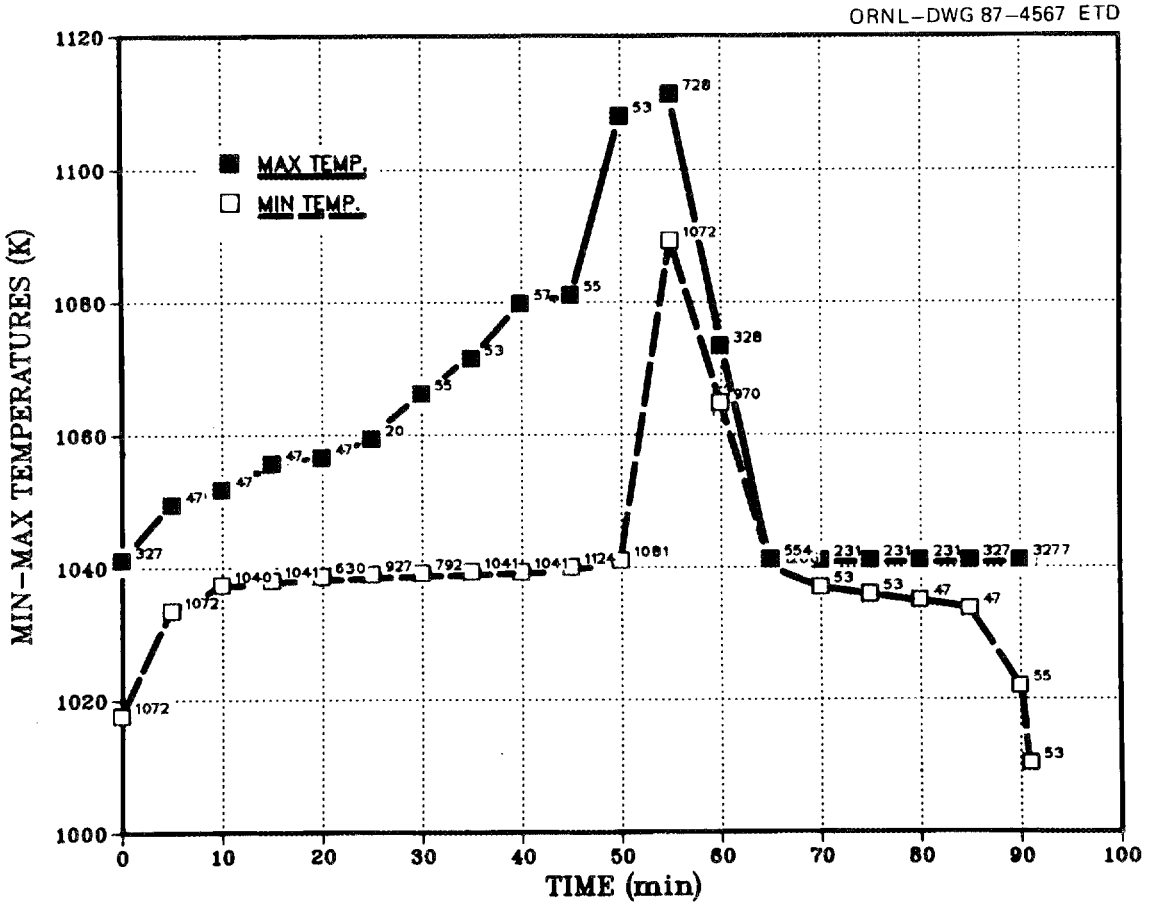

Fig. 13. Min-max temperature history, 1-g.

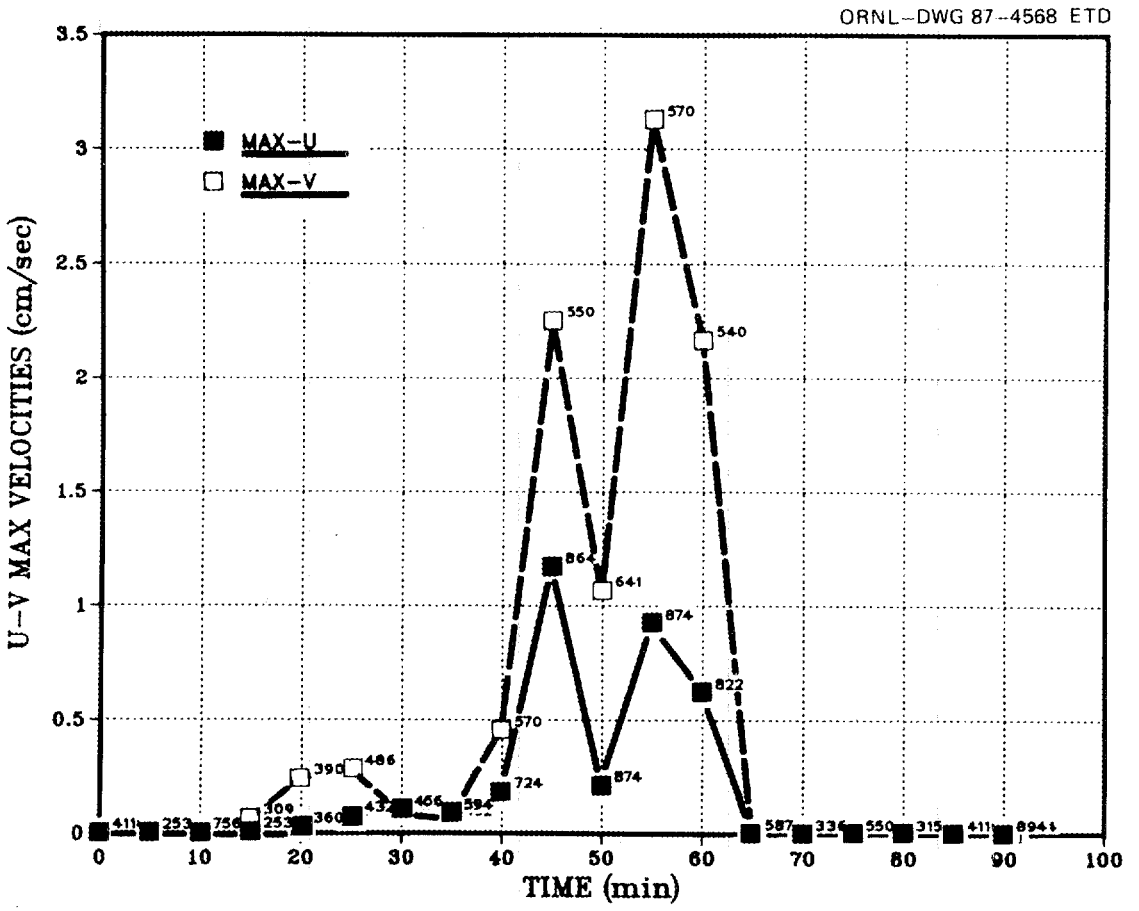

Fig. 14. Maximum U-V velocity history, 1-g.

a small 2-phase region occurring near the midplane. At this time, maximum temperatures reach 1105 K, well above the melting temperature.

Minimum and maximum temperatures are plotted in Fig. 13 for the 1-g cases. In general, maximum temperatures occur in the upper portion of the canister; minimum temperature tend to occur near the He tube and in the lower portions of the canister. It is noteworthy that a temperature range of up to 65 K may occur within the canister near the end of the heating cycle. Figure 14 shows that liquid velocities of up to 3 cm/s may appear briefly at a time approaching sunset when the extent of the liquid regime and the solar flux are at their peak.

Figures 15 through 22 illustrate the situation for the 0-g case. The orientation of the temperature and phase maps for this case is such that the maximum heat flux is assumed to occur at the top, opposite from the 1-g case. The principal differences relative to 1-g are due to the absence of gravity-driven liquid flows and the location of the void in the region of maximum heat flux. Figure pairs 15/16, 17/18, and 19/20 illustrate the temperature and phase fields at sunrise ($t = 0$) and at two times during the heating cycle, at $t = 30$ and 50min, the last time nearing the sunset condition. The absence of gravity causes a clearly altered behavior. Lower maximum velocities are achieved as a result of the smaller influence of surface tension variation along the void relative to density-driven flow in 1-g. Comparison of Figs. 14 and 22 illustrates that maximum velocities in 1-g may reach 3 cm/s briefly at sunset, compared with only 0.5 cm/s for the 0-g case. As a result, thermal convection is lower in 0-g which, combined with the location of the maximum heat zone opposite the void, generates more extreme temperatures compared with the 1-g case. Maximum temperatures reach 1150 K, ~40 K higher than in 1-g, and high temperatures in the range of 1100 K tend to persist for longer periods of time, as seen from the comparison of Figs. 13 and 21. However, comparison of the corresponding phase maps in 1-g and 0-g show quite similar patterns of liquid, solid, mushy, and void fields for the two cases.

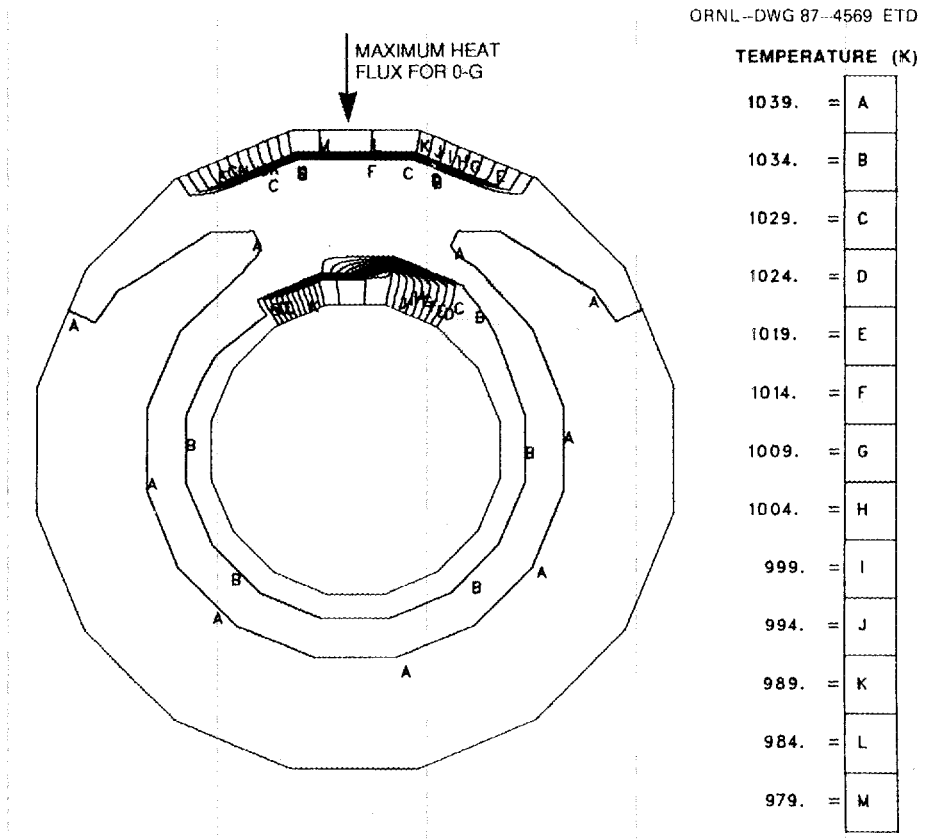

Fig. 15. Temperature contours — 0-g, sunrise (t = 0).

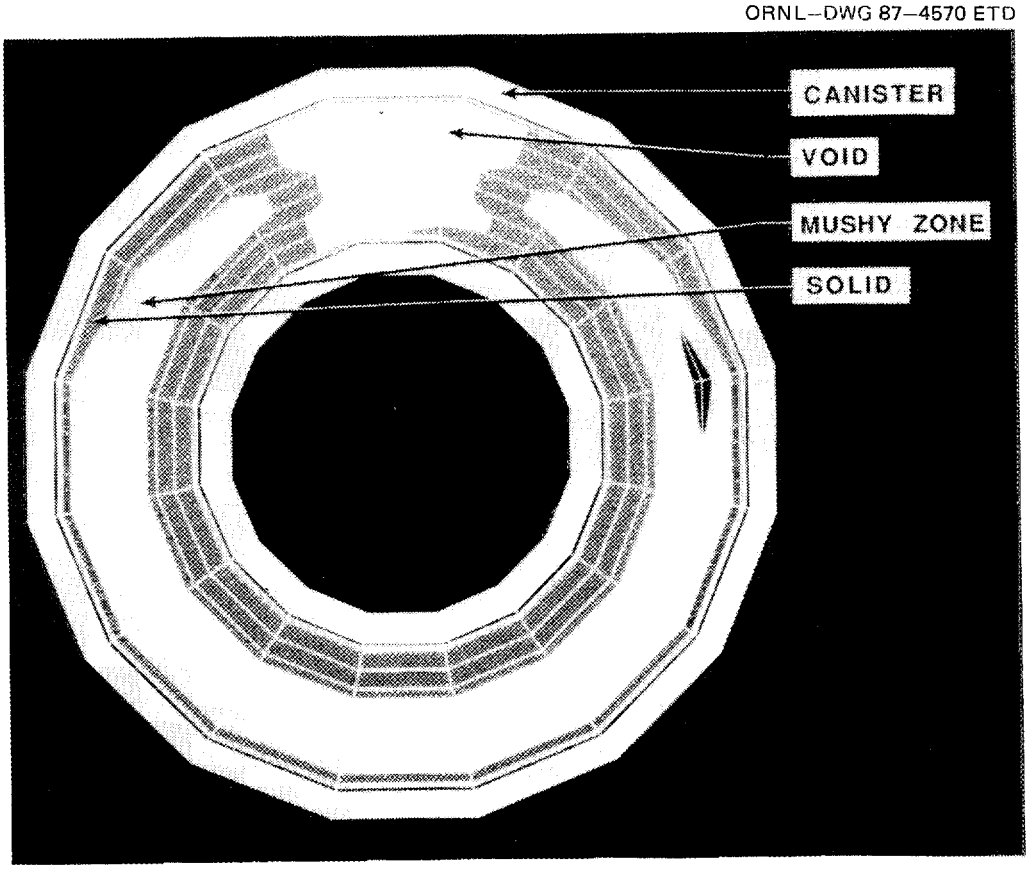

Fig. 16. Phase map — 0-g, sunrise (t = 0)

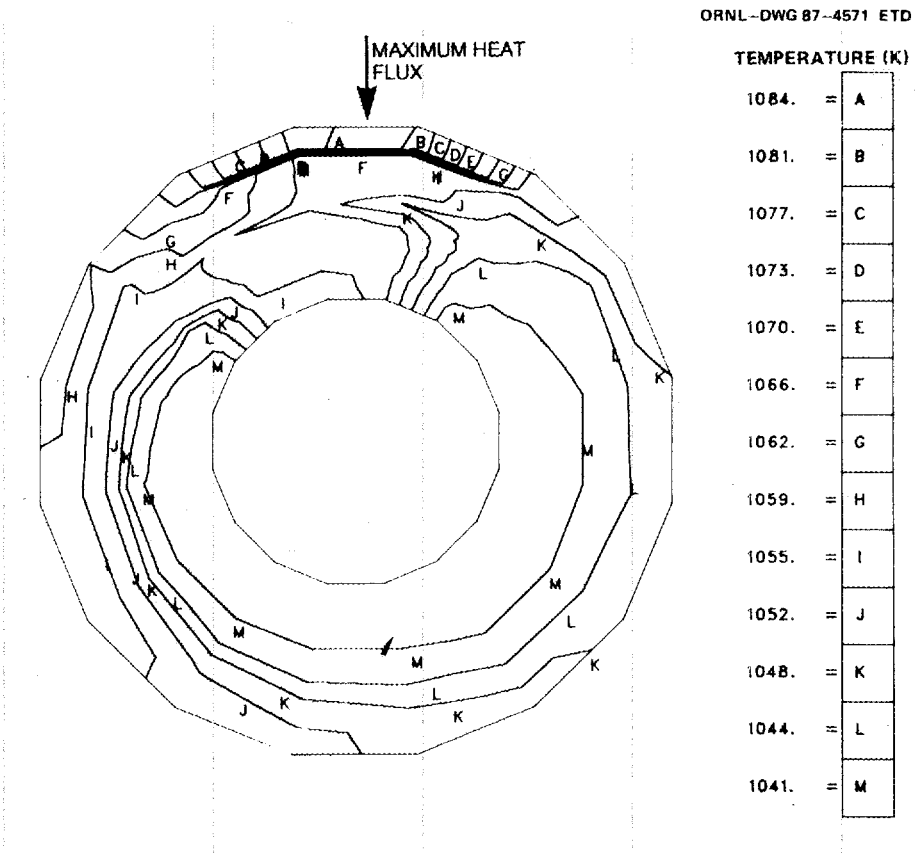

Fig. 17. Temperature contours — 0-g, t = 30 min.

ORNL-DWG 87-4572 ETD

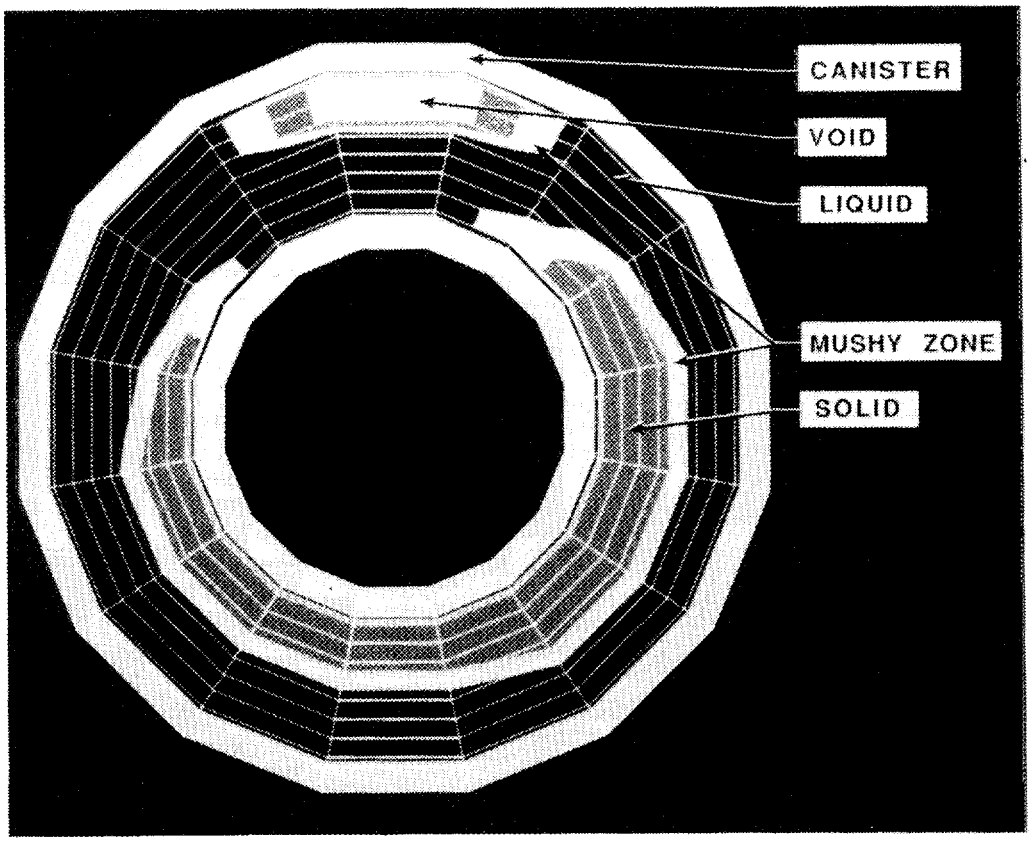

Fig. 18. Phase map — 0-g, t = 30 min.

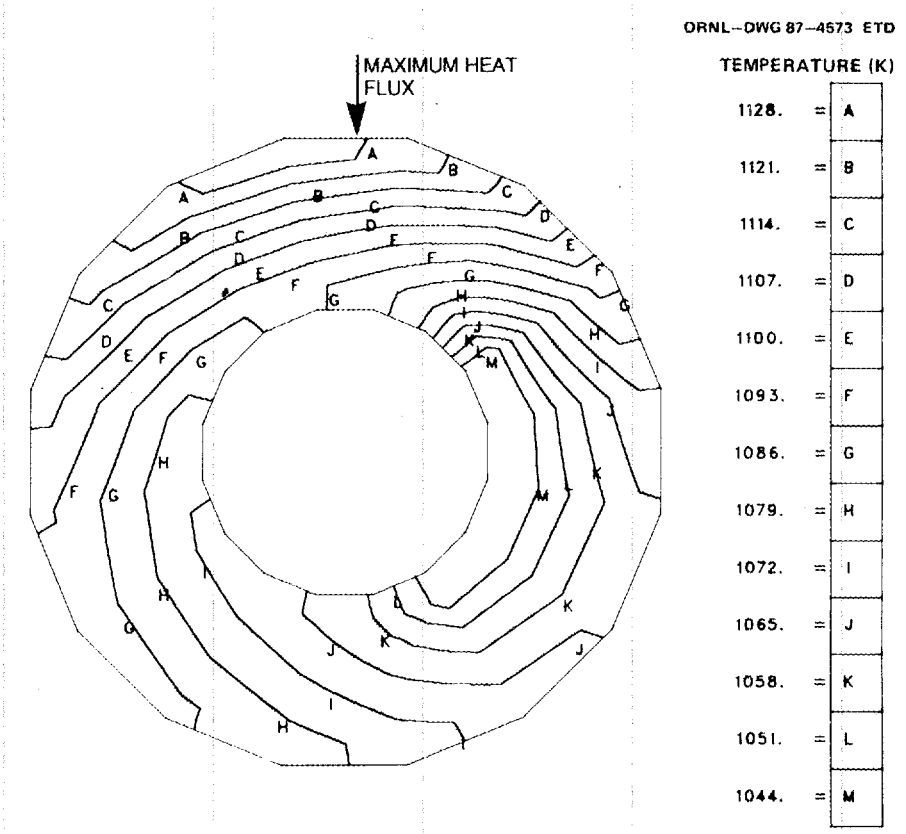

Fig. 19. Temperature contours — 0-g, t = 50 min (sunset).

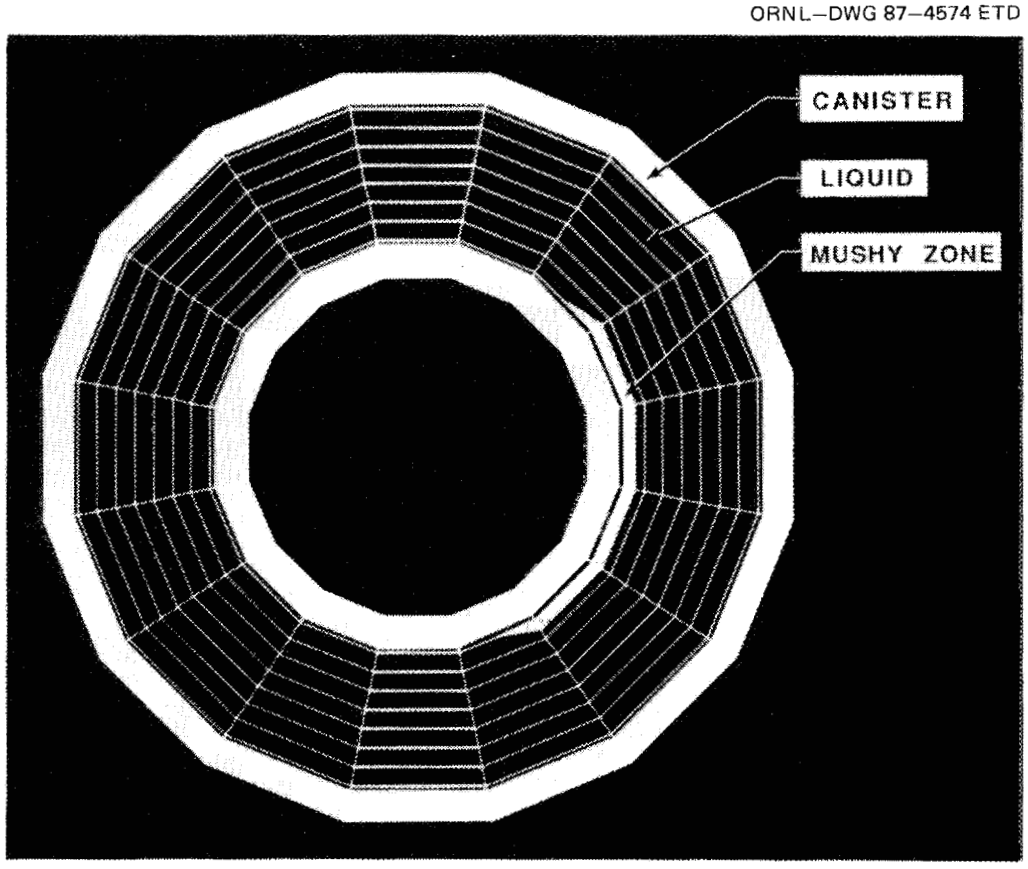

Fig. 20. Phase map — 0-g, t = 50 min (sunset).

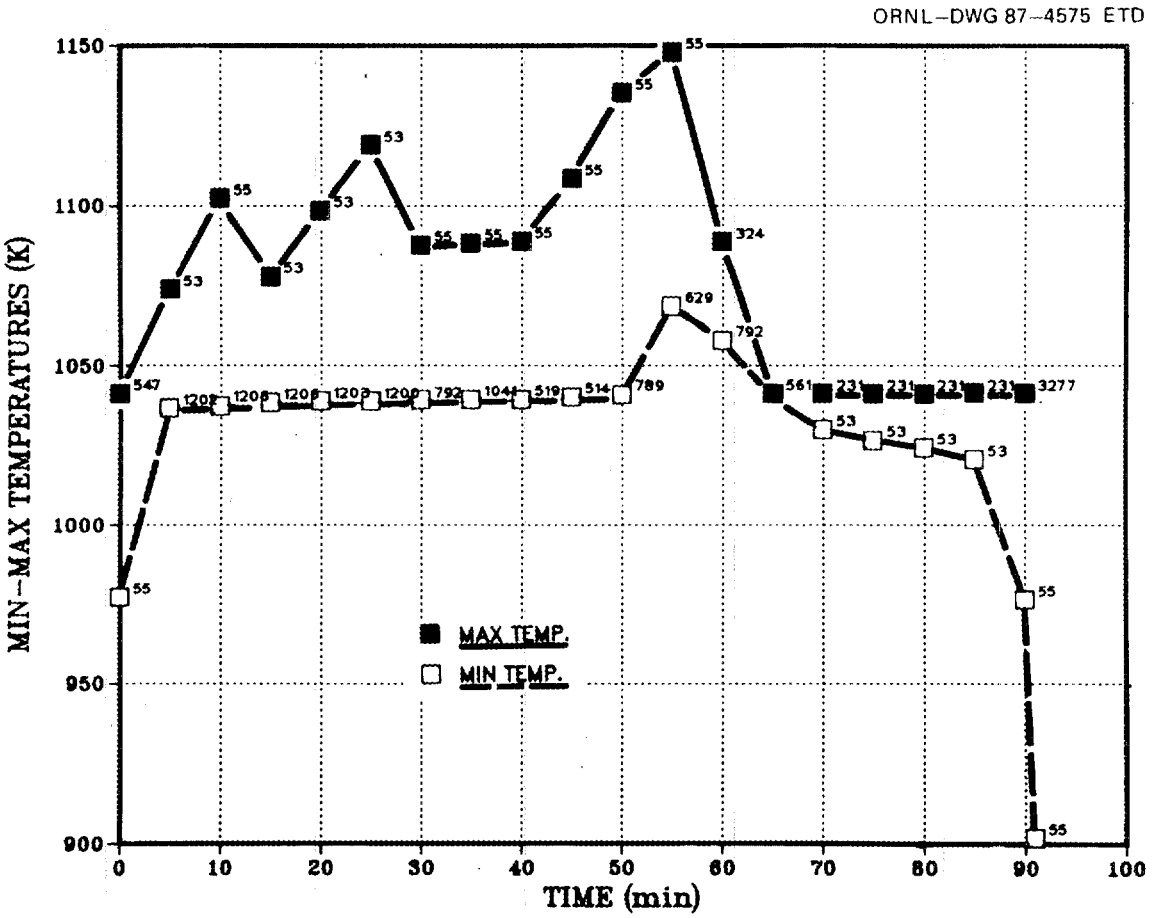

Fig. 21. Min-max temperature history, 0-g.

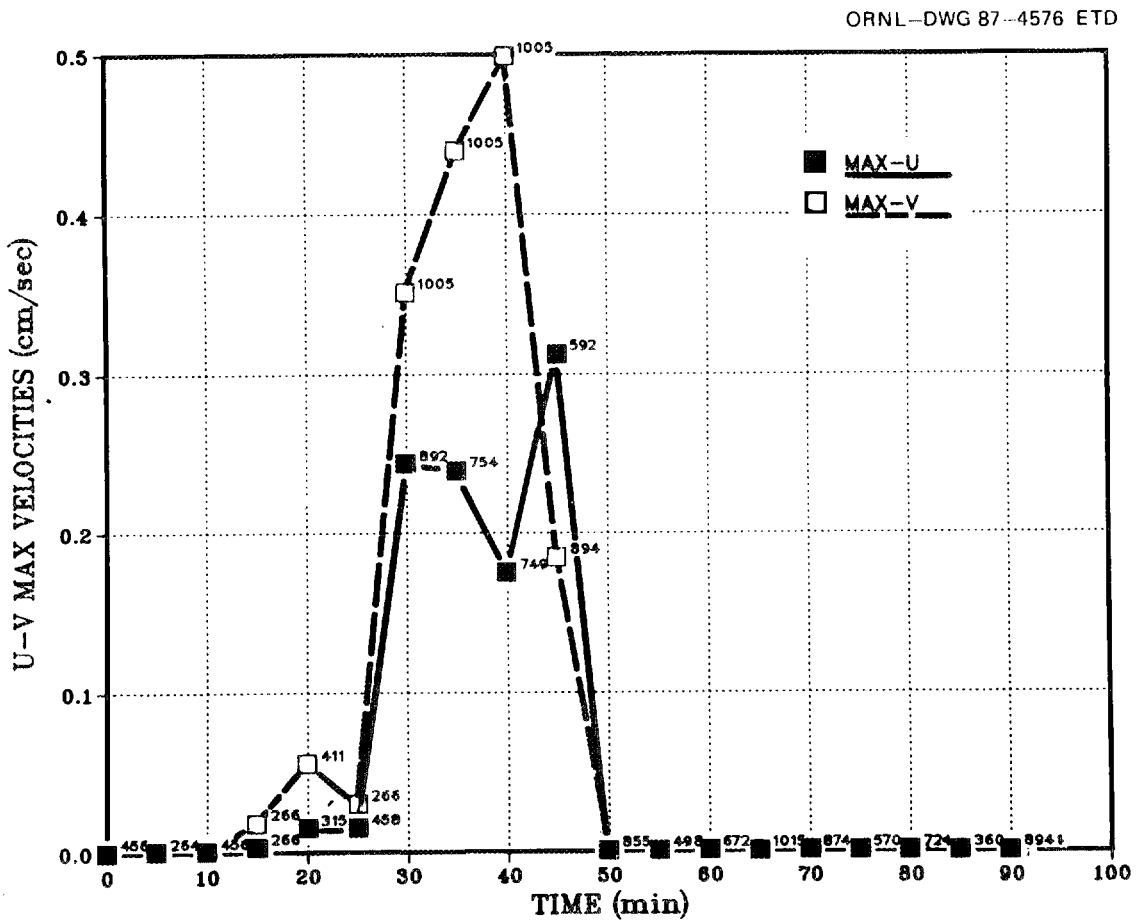

Fig. 22. U-V velocity history, 0-g.

6. CLOSING

This first phase of a thermal analysis of heat storage canisters used in receivers associated with solar dynamic power systems was directed toward an early identification of the vapor void effects on thermal profiles, and particularly the determination of any potential major 0-g effects. It was found that there could very well be significant differences in thermal behavior in 0-g relative to 1-g as a result of differences in both void behavior and the absence of bouyancy driven convection in 0-g. Recognition of these differences could perhaps lead to ground test designs which at least tend to minimize the differences. Whereas vapor voids in 1-g would likely be narrow, lens-shaped volumes located along the highest elevation surface permitted by the solidification front, voids developed in 0-g would tend to migrate to the region of highest temperature and assume a spherical shape as permitted by the presence of solid boundaries. Radiant and evaporative heat transport may assume comparable importance for fluoride salt voids at these temperature levels, while heat conduction across the void appears to be much less significant.

The following phenomena were included in the analysis: thermal conduction in the canister and both solid and liquid salt, thermal convection in the liquid salt, void shape and location by means of an improvised procedure, radiant heat transfer across the void, and the movement of the solidification front, all subject to transient, θ-dependent boundary conditions. The interplay between these effects is often difficult to predict but appears to yield temperature patterns that are more complex than those of less detailed treatments. As a consequence, a more realistic appraisal is obtained of thermal stresses in the canister and hence also a more realistic appraisal of projected design lifetimes.

A number of approximations were made at this stage of the work which hopefully will be eliminated in the course of a development effort within NASA's Advanced Solar Dynamic Program. A two-dimensional cylindrical coordinates approach as described here was deemed to be an

essential development step despite the recognition that the physical situation is strongly three-dimensional. Heat flow in the canister, particularly the radial sidewalls, and void shape and location call for treatment in three dimensions. Two dimensional treatment of these aspects entails some uncertain compromises with actual behavior. At the present time, we are attempting to perform the analysis in three dimensional cylindrical coordinates in conjunction with a more satisfactory method for predicting void shape and location.

7. NOMENCLATURE

e	average specific enthalpy in control volume, J/g
E	enthalpy in control volume, J
h	average volumetric enthalpy in control element, J/cm^3
ΔH_m	heat of fusion, J/g
J	molar flux, $mol/cm^2 \cdot sec$
k	thermal conductivity
k_e	effective thermal conductivity
M_w	molecular weight
P	pressure
Pr	Prandtl no.
q	heat flux, W/cm^2
r	radial coordinate
Ra	Rayleigh no.
T	temperature
t	cycle time from sunrise
u	r-velocity
U	θ-velocity
v	specific volume
V	control element volume

Subscripts

i	r-coordinate
j	θ-coordinate
m	mean value or melt temperature

Superscripts

S	solid
L	liquid
m	mushy zone

Greek Symbols

α	flow stability parameter
ρ	density
θ	cylindrical coordinate

8. REFERENCES

1. Preliminary Analysis and Design Document DR-02, Prepared for NASA-LeRC by Rocketdyne Div. of Rockwell International, Contract No. NAS3-24666 (Dec. 1986).

2. Steve Johnson, NASA LeRC, Personal communciations (May 1987).

3. A. D. Solomon, et al., *The Development of a Simulation Code for a Latent Heat Energy Storage System in a Space Station*, ORNL-6213, Oak Ridge National Laboratory, April 1986.

4. A. D. Solomon, *Mathematical Modeling of Phase Change Processes for Latent Heat Thermal Energy Storage*, ORNL/CSD-39, Oak Ridge National Laboratory (1979).

5. P. A. Gnadt, *Filling Heat Storage Tubes for Solar Brayton Cycle Heat Receiver with LiF*, ORNL-TM-2732, Oak Ridge National Laboratory (1970).

6. A. G. Martin, *Casting of LiH*, Y-1318 (1960).

7. *Brayton Cycle Cavity Design Receiver Study*, TRW Power Systems, NASA CR-54752 (1965).

8. J. M. Papazian et al., "Bubble Behavior During Solidification in Low Gravity," *AIAA Journal* 17, 1111-1117 (1979).

9 J. L. McGrew and B. K. Larkin, *Cryogenic Liquid Experiments in Orbit; Vol. II: Bubble Mechanics and Boiling*, NASA CR-652 (1968).

10. R. L. Thompson et al., "Marangoni Bubble Motion Phenomenon in Zero-Gravity," *Chem. Eng. Commun.* 5, 299-314 (1980).

11. E. P. Symons, *Zero-Gravity Equilibrium Configuration of Liquid-Vapor Interface In Toroidal Tanks*, NASA TN D-6076 (1970).

12. T. K. Sherwood et al., *Mass Transfer*, p. 182, McGraw-Hill, 1975.

13. G. J. Janz et al., *Physical Property Data Compilations Relevant to Energy Storage. II. Molten Salts*, NSRDS-NBS-61, part II.

14. R. D. Present, *Kinetic Theory of Gases*, Chapter 3, McGraw-Hill (1958).

15. C. Liu et al., "Natural Convection Heat Transfer in Long, Horizontal Cylindrical Annuli," *Int. Dev. in Heat Transfer*, ASME, 5, 976-984 (1961).

16. T. Manakata and I. Tanasawa, "Bouyancy and Surface Tension Driven Natural Convection with Solidification," in *Heat Transfer 1986*, Vol. 4, 1733-1738 (1986).

17. A. J. Chorin, "A Numerical Method for Solving Incompressible Viscous Flow Problems," *J. Comp. Phys. 2*, pp. 12-26 (1967).

18. J. B. Drake, *Incompressible Fluid Flow Calculation in the Presence of Voids and Liquid-Solid Phase Change* (to be published).

19. A. A. Amsden and F. H. Harlow, *The SMAC Method: A Numerical Technique for Calculating Incompressible Fluid Flows*, Los Alamos Scientific Laboratory Technical Report LA-4370 (1970).

20. J. M. Coulson, J. F. Richardson, *Chemical Engineering*, Vol. 2, Pergamon Press (1968).

21. G. J. Janz et al., "Physical Property Data Compilations Relative to Energy Storage," NSRDS-NBS 61, Part II (1979).

Internal Distribution

1. V. Alexiades
2. D. E. Bartine
3-4. J. Drake
5. R. C. Gwaltney
6. H. W. Hoffman
7. D. G. Morris
8. J. P. Nichols
9. M. Olszewski
10. M. Siman-Tov
11-12. A. Solomon
13. J. J. Tomlinson
14. H. E. Trammell
15-18. R. P. Wichner
19-20. P. T. Williams
21. D. G. Wilson
22. G. L. Yoder
23. ORNL Patent Office
24. Central Research Library
25. Document Reference Section
26-27. Laboratory Records Department
28. Laboratory Records (RC)

External Distribution

29-30. Steve Johnson, NASA Lewis Research Center, MS-501-13, 21000 Brookpark Road, Cleveland, OH 44135
31. Bob Migra, NASA Lewis Research Center, MS-301-3, 21000 Brookpark Road, Cleveland, OH 44135
32-33. Ted Mroz, NASA Lewis Research Center, MS-301-3, 21000 Brookpark Road, Cleveland, OH 44135
34. Office of Assistant Manager for Energy Research and Development, DOE-ORO, Oak Ridge, TN 37831
35-44. Office of Scientific and Technical Information, P.O. Box 62, Oak Ridge, TN 37831